

000 001 002 003 004 005 CONFORMAL CONFIDENCE SETS FOR BIOMEDICAL 006 IMAGE SEGMENTATION 007 008 009

010 **Anonymous authors**
 011 Paper under double-blind review
 012
 013
 014
 015
 016
 017
 018
 019
 020
 021
 022
 023
 024

ABSTRACT

025 We develop confidence sets which provide spatial uncertainty guarantees for the
 026 output of a black-box machine learning model designed for image segmentation.
 027 To do so we adapt conformal inference to the imaging setting, obtaining thresh-
 028 olds on a calibration dataset based on the distribution of the maximum of the
 029 transformed logit scores within and outside of the ground truth masks. We prove
 030 that these confidence sets, when applied to new predictions of the model, are guar-
 031 anteed to contain the true unknown segmented mask with desired probability. We
 032 show that learning appropriate score transformations on an *independent* learning
 033 dataset before performing calibration is crucial for optimizing performance. *We*
 034 *illustrate and validate our approach on polyps colonoscopy, brain imaging datasets*
 035 *and teeth datasets. To do so we obtain the logit scores from deep neural networks*
 036 *trained for polyps, brain mask and tooth segmentation segmentation. We show*
 037 *that using using distance and other transformations of the logit scores allows us*
 038 *to provide tight inner and outer confidence sets for the true masks whilst control-*
 039 *ling the false coverage rate.*

040 1 INTRODUCTION

041 Deep neural networks promise to significantly enhance a wide range of important tasks in biomed-
 042 ical imaging. However these models, as typically used, lack formal uncertainty guarantees on their
 043 output which can lead to overconfident predictions and critical errors (Guo et al., 2017; Gupta et al.,
 044 2020). Misclassifications or inaccurate segmentations can lead to serious consequences, includ-
 045 ing misdiagnosis, inappropriate treatment decisions, or missed opportunities for early intervention
 046 (Topol, 2019). Without uncertainty quantification, medical professionals cannot rely on deep learn-
 047 ing models to provide accurate information and predictions which can limit their use in practical
 048 applications (Jungo et al., 2020).

049 In order to address this problem, conformal inference, a robust framework for uncertainty quan-
 050 tification, has become increasingly used as a means of providing prediction guarantees, offering
 051 reliable, distribution-free confidence sets for the output of neural networks which have finite sample
 052 validity. This approach, originally introduced in Papadopoulos et al. (2002); Vovk et al. (2005),
 053 has become increasingly popular due to its ability to provide rigorous statistical guarantees without
 054 making strong assumptions about the underlying data distribution or model architecture. Conformal
 055 prediction methods, in their most commonly used form - split conformal inference - work by cali-
 056 brating the predictions of the model on a held-out dataset in order to provide sets which contain the
 057 output with a given probability, see Shafer & Vovk (2008) and Angelopoulos & Bates (2021) for
 058 good introductions.

059 In the context of image segmentation, we have a decision to make at each pixel/voxel of an im-
 060 age which can lead to a large multiple testing problem. Traditional conformal methods, typically
 061 designed for scalar outputs, require adaptation to handle multiple tests and their inherent spatial
 062 dependencies. To do so Angelopoulos et al. (2021) applied conformal inference pixelwise and per-
 063 formed multiple testing correction on the resulting p -values, however this approach does not account
 064 for the complex dependence structure inherent in the images. To take advantage of this structure, in
 065 an approach analogous to the *False discovery rate (FDR)* control of (Benjamini & Hochberg, 1995),
 066 Bates et al. (2021) and Angelopoulos et al. (2024) sought to control the expected risk of a given
 067 loss function over the image and used a conformal approach to produce outer confidence sets for

054 segmented images which control the expected proportion of false negatives. Other work considering
 055 conformal inference in the context of multiple dependent hypotheses includes Marandon (2024) and
 056 Blanchard et al. (2024) who established conformal FDR control when testing for the presence of
 057 missing links in graphs.

058 In this work we argue that bounding the segmented outcome with guarantees in probability rather
 059 than on the proportion of discoveries is more informative, avoiding errors at the borders of potential
 060 growths/tumors. This is analogous to the tradeoff between *familywise error rate (FWER)* and *FDR*
 061 control in the multiple testing literature in which there is a balance between power and coverage
 062 rate, (*a correspondence which we formalize in Section A.8*). The distinction is that in medical im-
 063 age segmentation making mistakes can have potentially serious consequences Under-segmentation
 064 might cause part of the true mask to be missed, potentially leading to inadequate treatment (Jalalifar
 065 et al., 2022). Over-segmentation, on the other hand, could result in unnecessary interventions, in-
 066 creasing patient risk and healthcare costs (Gupta et al., 2020; Patz et al., 2014). Confidence sets are
 067 instead guaranteed to contain the outcome with a given level of certainty. Since the guarantees are
 068 more meaningful the problem is more difficult and existing work on conformal uncertainty quan-
 069 tification for images has thus often focused on producing sets with guarantees on the proportions
 070 of discoveries or pixel level inference rather than coverage (Bates et al. (2021), Wieslander et al.
 071 (2020), Mossina et al. (2024)) which is a stricter error criterion.

072 In order to obtain confidence sets we use a split-conformal inference approach in which we learn
 073 appropriate cutoffs, with which to threshold the output of an image segmenter, from a calibration
 074 dataset. These thresholds are obtained by considering the distribution of the maximum logit (trans-
 075 formed) scores provided by the model within and outside of the ground truth masks. This approach
 076 allows us to capture the spatial nature of the uncertainty in segmentation tasks, going beyond simple
 077 pixel-wise confidence measures. By applying these learned thresholds to new predictions, we can
 078 generate inner and outer confidence sets that are guaranteed to contain the true, unknown segmented
 079 mask with a desired probability. As we shall see, naively using the original model scores to do so
 080 can lead to rather large and uninformative outer confidence sets but these can be greatly improved
 081 using distance transformations.

082 2 THEORY

084 2.1 SET UP

086 Let $\mathcal{V} \subset \mathbb{R}^m$, for some dimension $m \in \mathbb{N}$, be a finite set corresponding to the domain which
 087 represents the pixels/voxels/points at which we observe imaging data. Let $\mathcal{X} = \{g : \mathcal{V} \rightarrow \mathbb{R}\}$ be
 088 the set of real functions on \mathcal{V} and let $\mathcal{Y} = \{g : \mathcal{V} \rightarrow \{0, 1\}\}$ be the set of all functions on \mathcal{V} taking
 089 the values 0 or 1. We shall refer to elements of \mathcal{X} and \mathcal{Y} as images. Suppose that we observe a
 090 calibration dataset $(X_i, Y_i)_{i=1}^n$ of random images, where $X_i : \mathcal{V} \rightarrow \mathbb{R}$ represents the i th observed
 091 calibration image and $Y_i : \mathcal{V} \rightarrow \{0, 1\}$ outputs labels at each $v \in \mathcal{V}$ giving 1s at the true location
 092 of the objects in the image X_i that we wish to identify and 0s elsewhere. Let $\mathcal{P}(\mathcal{V})$ be the set of all
 093 subsets of \mathcal{V} . Given a function $f : \mathcal{X} \rightarrow \mathcal{X}$, we shall write $f(X, v)$ to denote $f(X)(v)$ for all $v \in \mathcal{V}$.

094 Let $s : \mathcal{X} \rightarrow \mathcal{X}$ be a score function - trained on an independent dataset - such that given an image
 095 pair $(X, Y) \in \mathcal{X} \times \mathcal{Y}$, $s(X)$ is a score image in which $s(X, v)$ is intended to be higher at the $v \in \mathcal{V}$
 096 for which $Y(v) = 1$. The score function can for instance be the logit scores obtained from applying
 097 a deep neural network image segmentation method to the image X . Given $X \in \mathcal{X}$, let $\hat{M}(X) \in \mathcal{Y}$
 098 be the predicted mask given by the model which is assumed to be obtained using the scores $s(X)$.

099 In what follows we will use the calibration dataset to construct confidence functions $I, O : \mathcal{X} \rightarrow$
 100 $\mathcal{P}(\mathcal{V})$ such that for a new image pair (X, Y) , given error rates $\alpha_1, \alpha_2 \in (0, 1)$ we have

$$101 \quad \mathbb{P}(I(X) \subseteq \{v \in \mathcal{V} : Y(v) = 1\}) \geq 1 - \alpha_1, \quad (1)$$

$$103 \quad \text{and } \mathbb{P}(\{v \in \mathcal{V} : Y(v) = 1\} \subseteq O(X)) \geq 1 - \alpha_2. \quad (2)$$

104 Here $I(X)$ and $O(X)$ serve as inner and outer confidence sets for the location of the true segmented
 105 mask. Their interpretation is that, up to the guarantees provided by the probabilistic statements (1)
 106 and (2), we can be sure that for each $v \in I(X)$, $Y(v) = 1$ or that for each $v \notin O(X)$, $Y(v) = 0$.
 107 Joint control over the events can also be guaranteed, either via sensible choices of α_1 and α_2 or by
 108 using the joint distribution of the maxima of the logit scores - see Section 2.3.

In order to establish conformal confidence results we shall require the following exchangeability assumption.

Assumption 1. Given a new random image pair, (X_{n+1}, Y_{n+1}) , suppose that $(X_i, Y_i)_{i=1}^{n+1}$ is an exchangeable sequence of random image pairs in the sense that

$$\{(X_1, Y_1), \dots, (X_{n+1}, Y_{n+1})\} =_d \{(X_{\sigma(1)}, Y_{\sigma(1)}), \dots, (X_{\sigma(n+1)}, Y_{\sigma(n+1)})\}$$

for all permutations $\sigma \in S_{n+1}$. Here $=_d$ denotes equality in distribution and S_{n+1} is the group of permutations of the integers $\{1, \dots, n+1\}$.

Exchangeability or a variant is a standard assumption in the conformal inference literature (Angelopoulos & Bates, 2021) and facilitates coverage guarantees. It holds for instance if we assume that the collection $(X_i, Y_i)_{i=1}^{n+1}$ is an i.i.d. sequence of image pairs but is more general and in principle allows for other dependence structures.

2.2 MARGINAL CONFIDENCE SETS

In order to construct conformal confidence sets let $f_I, f_O : \mathcal{X} \rightarrow \mathcal{X}$ be inner and outer transformation functions and for each $1 \leq i \leq n+1$, let $\tau_i = \max_{v \in \mathcal{V}: Y_i(v)=0} f_I(s(X_i), v)$ and $\gamma_i = \max_{v \in \mathcal{V}: Y_i(v)=1} -f_O(s(X_i), v)$ be the maxima of the function transformed scores over the areas at which the true labels equal 0 and 1 respectively. We will require the following assumption on the scores and the transformation functions.

Assumption 2. (Independence of scores) $(X_i, Y_i)_{i=1}^{n+1}$ is independent of the functions s, f_O, f_I .

Given this we construct confidence sets as follows.

Theorem 2.1. (*Marginal inner set*) Under Assumptions 1 and 2, given $\alpha_1 \in (0, 1)$, let

$$\lambda_I(\alpha_1) = \inf \left\{ \lambda : \frac{1}{n} \sum_{i=1}^n \mathbb{1}[\tau_i \leq \lambda] \geq \frac{\lceil (1 - \alpha_1)(n + 1) \rceil}{n} \right\},$$

and define $I(X) = \{v \in \mathcal{V} : f_I(s(X), v) > \lambda_I(\alpha_1)\}$. Then,

$$\mathbb{P}(I(X_{n+1}) \subseteq \{v \in \mathcal{V} : Y_{n+1}(v) = 1\}) \geq 1 - \alpha_1. \quad (3)$$

Proof. Under Assumptions 1 and 2, exchangeability of the image pairs implies exchangeability of the sequence $(\tau_i)_{i=1}^{n+1}$. In particular, $\lambda_I(\alpha_1)$ is the upper α_1 quantile of the distribution of $(\tau_i)_{i=1}^n \cup \{\infty\}$ and so, by Lemma 1 of Tibshirani et al. (2019), it follows that

$$\mathbb{P}(\tau_{n+1} \leq \lambda_I(\alpha_1)) \geq 1 - \alpha_1.$$

Now consider the event that $\tau_{n+1} \leq \lambda_I(\alpha_1)$. On this event, $f_I(s(X_{n+1}), v) \leq \lambda_I(\alpha_1)$ for all $v \in \mathcal{V}$ such that $Y_{n+1}(v) = 0$. As such, given $u \in \mathcal{V}$ such that $f_I(s(X_{n+1}), u) > \lambda_I(\alpha_1)$, we must have $Y_{n+1}(u) = 1$ and so $I(X_{n+1}) \subseteq \{v \in \mathcal{V} : Y_{n+1}(v) = 1\}$. It thus follows that

$$\mathbb{P}(I(X_{n+1}) \subseteq \{v \in \mathcal{V} : Y_{n+1}(v) = 1\}) \geq \mathbb{P}(\tau_{n+1} \leq \lambda_I(\alpha_1)) \geq 1 - \alpha_1.$$

□

For the outer set we have the following analogous result.

Theorem 2.2. (*Marginal outer set*) Under Assumptions 1 and 2, given $\alpha_2 \in (0, 1)$, let

$$\lambda_O(\alpha_2) = \inf \left\{ \lambda : \frac{1}{n} \sum_{i=1}^n \mathbb{1}[\gamma_i \leq \lambda] \geq \frac{\lceil (1 - \alpha_2)(n + 1) \rceil}{n} \right\},$$

and define $O(X) = \{v \in \mathcal{V} : -f_O(s(X), v) \leq \lambda_O(\alpha_2)\}$. Then,

$$\mathbb{P}(\{v \in \mathcal{V} : Y_{n+1}(v) = 1\} \subseteq O(X_{n+1})) \geq 1 - \alpha_2. \quad (4)$$

Proof. Arguing as in the proof of Theorem 2.1, it follows that $\mathbb{P}(\gamma_{n+1} \leq \lambda_O(\alpha_2)) \geq 1 - \alpha_2$. Now on the event that $\gamma_{n+1} \leq \lambda_O(\alpha_2)$ we have $-f_O(s(X_{n+1}), v) \leq \lambda_O(\alpha_2)$ for all $v \in \mathcal{V}$ such that $Y_{n+1}(v) = 1$. As such, given $u \in \mathcal{V}$ such that $-f_O(s(X_{n+1}), u) > \lambda_O(\alpha_2)$, we must have $Y_{n+1}(u) = 0$ and so $O(X)^C \subseteq \{v \in \mathcal{V} : Y_{n+1}(v) = 0\}$. The result then follows as above. □

Remark 2.3. We have used the maximum over the transformed scores in order to combine score information on and off the ground truth masks. The maximum is a natural combination function in imaging and is commonly used in the context of multiple testing (Worsley et al., 1992). However the theory above is valid for any increasing combination function. We show this in Appendix A.1 where we establish generalized versions of these results.

Remark 2.4. Inner and outer coverage can also be viewed as a special case of conformal risk control with an appropriate choice of loss function. We can thus instead establish coverage results as a corollary to risk control, see Appendix A.2 for details. This amounts to an alternative proof of the results as the proof of the validity of risk control is different though still strongly relies on exchangeability.

2.3 JOINT CONFIDENCE SETS

Instead of focusing on marginal control one can instead spend all of the α available to construct sets which have a joint probabilistic guarantees. This gain comes at the expense of a loss of precision. The simplest means of constructing jointly valid confidence sets is via the marginal sets themselves.

Corollary 2.5. (Joint from marginal) Assume Assumptions 1 and 2 hold and given $\alpha \in (0, 1)$ and $\alpha_1, \alpha_2 \in (0, 1)$ such that $\alpha_1 + \alpha_2 \leq \alpha$, define $I(X)$ and $O(X)$ as in Theorems 2.1 and 2.2. Then

$$\mathbb{P}(I(X_{n+1}) \subseteq \{v \in \mathcal{V} : Y_{n+1}(v) = 1\} \subseteq O(X_{n+1})) \geq 1 - \alpha. \quad (5)$$

Alternatively joint control can be obtained using the joint distribution of the maxima of the transformed logit scores as follows.

Theorem 2.6. (Joint coverage) Assume that Assumption 1 and 2 hold. Given $\alpha \in (0, 1)$, define

$$\lambda(\alpha) = \inf \left\{ \lambda : \frac{1}{n} \sum_{i=1}^n \mathbb{1}[\max(\tau_i, \gamma_i) \leq \lambda] \geq \frac{\lceil (1-\alpha)(n+1) \rceil}{n} \right\}.$$

Let $O(X) = \{v \in \mathcal{V} : -f_O(s(X), v) \leq \lambda(\alpha)\}$ and $I(X) = \{v \in \mathcal{V} : f_I(s(X), v) > \lambda(\alpha)\}$. Then,

$$\mathbb{P}(I(X_{n+1}) \subseteq \{v \in \mathcal{V} : Y_{n+1}(v) = 1\} \subseteq O(X_{n+1})) \geq 1 - \alpha. \quad (6)$$

Proof. Exchangeability of the image pairs implies exchangeability of the sequence $(\tau_i, \gamma_i)_{i=1}^{n+1}$. Moreover on the event that $\max(\tau_{n+1}, \gamma_{n+1}) \leq \lambda(\alpha)$ we have $\tau_{n+1} \leq \lambda(\alpha)$ and $\gamma_{n+1} \leq \lambda(\alpha)$ so the result follows via a proof similar to that of Theorems 2.1 and 2.2. \square

Remark 2.7. The advantage of Corollary 2.5 is that the resulting inner and outer sets provide pivotal inference - not favouring one side or the other - which can be important when the distribution of the score function is asymmetric. Moreover the levels α_1 and α_2 can be used to provide a greater weight to either inner or outer sets whilst maintaining joint coverage. Theorem 2.6 may instead be useful when there is strong dependence between τ_{n+1} and γ_{n+1} . However, when this dependence is weak, scale differences in the scores can lead to a lack of pivotality. This can be improved by appropriate choices of the score transformations f_I and f_O however in practice it may be simpler to construct joint sets using Corollary 2.5.

2.4 OPTIMIZING SCORE TRANSFORMATIONS

The choice of score transformations f_I and f_O is extremely important and can have a large impact on the size of the conformal confidence sets. The best choice depends on both the distribution of the data and on the nature of the output of the image segmentor used to calculate the scores. We thus recommend setting aside a learning dataset independent from both the calibration dataset, used to compute the conformal thresholds, and the test dataset. This approach was used in Sun & Yu (2024) to learn the best copula transformation for combining dependent data streams.

In order to make efficient use of the data available, the learning dataset can in fact contain some or all of the data used to train the image segmentor. This data is assumed to be independent of the calibration and test data and so can be used to learn the best score transformations without compromising subsequent validity. The advantage of doing so is that less additional data needs to be set aside or collected for the purposes of learning a score function. Moreover it allows for additional

216 data to be used to train the model resulting in better segmentation performance. The disadvantage is
 217 that machine learning models typically overfit their training data meaning that certain score functions
 218 may appear to perform better on this data than they do in practice. The choice of whether to include
 219 training data in the learning dataset thus depends on the quantity of data available and the quality of
 220 the segmentation model.

221 A score transformation that we will make particular use of in Section 3 is based on the distance
 222 transformation which we define as follows. Given $\mathcal{A} \subseteq \mathcal{V}$, let $E(\mathcal{A})$ be the set of points on the
 223 boundary of \mathcal{A} obtained using the marching squares algorithm (Maple, 2003). Given a distance
 224 metric ρ define the distance transformation $d_\rho : \mathcal{P}(\mathcal{V}) \times \mathcal{V} \rightarrow \mathbb{R}$, which sends $\mathcal{A} \in \mathcal{P}(\mathcal{V})$ and $v \in \mathcal{V}$
 225 to

$$d_\rho(\mathcal{A}, v) = \text{sign}(\mathcal{A}, v) \min\{\rho(v, e) : e \in E(\mathcal{A})\},$$

226 where $\text{sign}(\mathcal{A}, v) = 1$ if $v \in \mathcal{A}$ and equals -1 otherwise. The function d_ρ is an adaption of the
 227 distance transform of Borgefors (1986) which provides positive values within the set \mathcal{A} and negative
 228 values outside of \mathcal{A} .

231 2.5 CONSTRUCTING CONFIDENCE SETS FROM BOUNDING BOXES

232 Existing work on conformal inner and outer confidence sets, which aim to provide coverage of
 233 the entire ground truth mask with a given probability, has primarily focused on bounding boxes
 234 (de Grancey et al., 2022; Andéol et al., 2023; Mukama et al., 2024). These papers adjust for mul-
 235 tiple comparisons over the 4 edges of the bounding box, doing so conformally by comparing the
 236 distance between the predicted bounding box and the bounding box of the ground truth mask. These
 237 approaches provide box-wise coverage by aggregating the predictions over all objects within all of
 238 the calibration images, often combining multiple bounding boxes per image. However, as observed
 239 in Section 5 of de Grancey et al. (2022), doing so violates exchangeability which is needed for valid
 240 conformal inference, as there is dependence between the objects within each image. Instead image-
 241 wise coverage can be provided without violating exchangeability by treating the union of the boxes
 242 as the ground truth image (de Grancey et al., 2022; Andéol et al., 2023).

243 We establish the validity of a version of the image-wise max-additive method of Andéol et al. (2023)
 244 (adapted to provide coverage of the ground truth) as a corollary to our results, see Appendix A.3.
 245 In this approach we define bounding box scores based on the chessboard distance transformation
 246 to the inner and outer predicted masks and use these scores to provide conformal confidence sets.
 247 Validity then follows as a consequence of the results above as we show in Corollaries A.5 and A.6.
 248 We compare to this approach in our experiments below. Targeting bounding boxes does not directly
 249 target the mask itself and so the resulting confidence sets are typically conservative.

251 3 APPLICATION TO POLYPS SEGMENTATION

252 In order to illustrate and validate our approach we consider the problem of polyps segmentation. To
 253 do so we use the same dataset as in Angelopoulos et al. (2024) in which 1798 polyps images, with
 254 available ground truth masks were combined from 5 open-source datasets (Pogorelov et al. (2017),
 255 Borgli et al. (2020) Bernal et al. (2012), Silva et al. (2014)). Logit scores were obtained for these
 256 images using the parallel reverse attention network (PraNet) model (Fan et al., 2020).

257 3.1 CHOOSING A SCORE TRANSFORMATION

258 In order to optimize the size of our confidence sets we set aside 298 of the 1798 polyps images
 259 to form a learning dataset on which to choose the best score transformations. Importantly as the
 260 learning dataset is independent of the remaining 1500 images set-aside, we can study it as much as
 261 we like without compromising the validity of the follow-up analyses in Sections 3.2. In particular
 262 in this section we shall use the learning dataset to both calibrate and study the results, in order to
 263 maximize the amount of important information we can learn from it.

264 The score transformations we considered were the identity (after softmax transformation) and dis-
 265 tance transformations of the predicted masks: taking $f_I(s(X), v) = f_O(s(X), v) = d_\rho(\hat{M}(X), v)$,
 266 where ρ is the Euclidean metric. We also compare to the results of using the bounding box transfor-
 267 mations $f_I = b_I$ and $f_O = b_O$ which correspond to transforming the predicted bounding box using

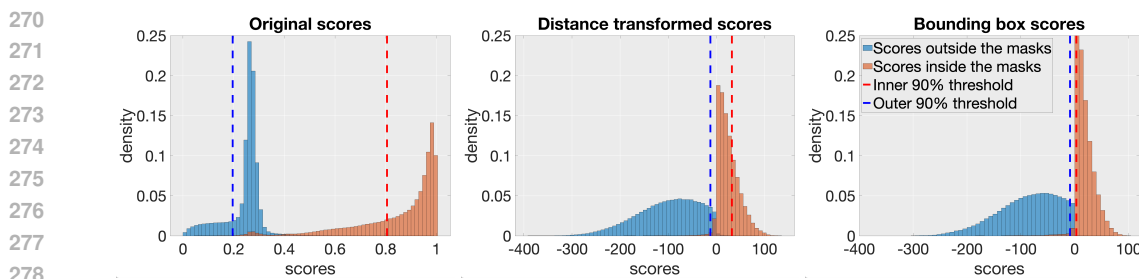


Figure 1: Histograms of the distribution of the scores over the whole image within and outside the ground truth masks. Thresholds obtained for the marginal 90% inner and outer confidence sets, obtained based on quantiles of the distribution of $(\tau_i)_{i=1}^n$ and $(\gamma_i)_{i=1}^n$, are displayed in red and blue.

a distance transformation based on the chessboard metric and are defined formally in Appendix A.3. For the purposes of plotting we used the combined bounding box scores defined in Definition A.4.

From the histograms in Figure 1 we can see that thresholding the original scores at the inner threshold well separates the data. However this is not the case for the outer threshold for which the data is better separated using the distance transformed and bounding box scores. Figure 2 shows PraNet scores for 2 typical examples, along with surface plots of the transformed scores and corresponding 90% marginal confidence regions (with thresholds obtained from calibrating over the learning dataset). From these we see that PraNet typically assigns a high softmax score to the polyps regions which decreases in the regions directly around the boundary before returning to a higher level away from the polyps. This results in tight inner sets but large outer sets as the model struggles to identify where the polyps ends. Instead the distance transformed and bounding box scores are much better at providing outer bounds on the polyps, with distance transformed scores providing a tighter outside fit. Additional examples are shown in Figures A8 and A9 and have the same conclusion.

Based on the results of the learning dataset we decided to combine the best of the approaches for the inner and outer sets respectively for the inference in Section 3.2, taking f_I to be the identity and f_O to be the distance transformation of the predicted mask in order to optimize performance. We can also use the learning dataset to determine how to weight the α used to obtain joint confidence sets. A ratio of 4 to 1 seems appropriate here in light of the fact that in this dataset identifying where a given polyps ends appears to be more challenging than identifying pixels where we are sure that there is a polyps. To achieve joint coverage of 90% this involves taking $\alpha_1 = 0.02$ and $\alpha_2 = 0.08$.

3.2 ILLUSTRATING THE PERFORMANCE OF CONFORMAL CONFIDENCE SETS

In order to illustrate the full extent of our methods in practice we divide the set aside 1500 images at random into 1000 for conformal calibration, and 500 for testing. The resulting conformal confidence sets for 10 example images from the test dataset are shown in Figure 3, with inner sets obtained using the original scores and outer sets using the distance transformed scores. The inner sets are shown in red and represent regions where we can have high confidence of the presence of polyps. The outer sets are shown in blue and represent regions in which the polyps may be. The ground truth mask for each polyps is shown in yellow and can be compared to the original images. In each of the examples considered the ground truth is bounded from within by the inner set and from without by the outer set. Results for confidence sets based on the original and bounding box scores as well as additional examples are available in Figures A10 and A11. Confidence sets can also be provided for the bounding boxes themselves if that is the object of interest, see Figure A12. Joint 90% confidence sets are displayed in Figure A13, from which we can see that with alpha-weighting (i.e. taking $\alpha_1 = 0.02$ and $\alpha_2 = 0.08$) we are able to obtain joint confidence sets which are still relatively tight.

These results collectively show that we can provide informative confidence bounds for the location of the polyps and allow us to use the PraNet segmentation model with uncertainty guarantees. From Figure 3 we can see that the method, which combines the original and the transformed scores, effectively delineates polyps regions. These results also help to make us aware of the limitations of the model, allowing medical practitioners to follow up on outer sets which do not contain inner sets in

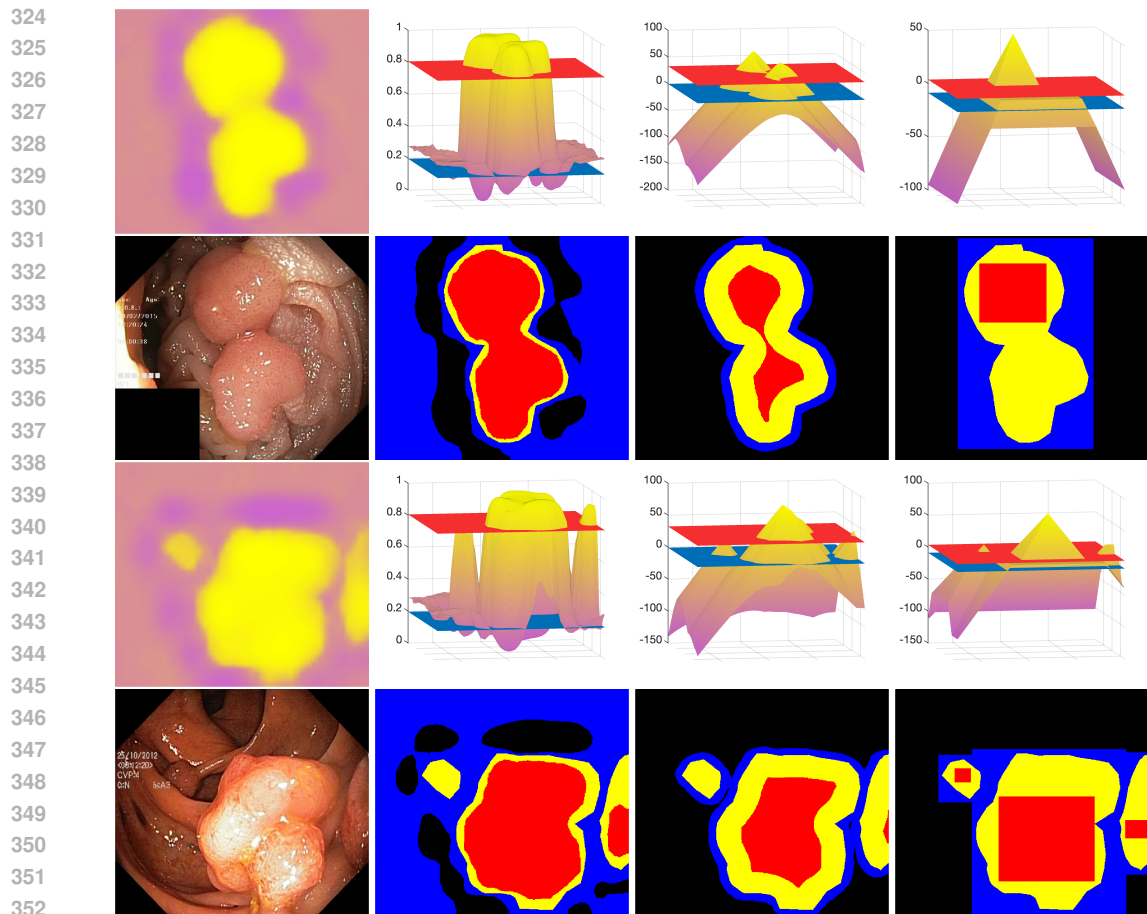


Figure 2: Illustrating the performance of the different score transformations on the learning dataset. We display 2 example polyps images and present the results of each in 8 panels. These panels are as follows. Bottom left: the original image of the polyps. Top Left: an intensity plot of the scores obtained from PraNet with purple/yellow indicating areas of lower/higher assigned probability. For the remaining panels, 3 different score transformations are shown which from left to right are the original scores, distance transformed scores $d_\rho(\hat{M}(X), v)$ and bounding box scores (obtained using the combined bounding box score b_M defined in Definition A.4). In each of the panels on the top row a surface plot of the transformed PraNet scores is shown, along with the conformal thresholds which are used to obtain the marginal 90% inner and outer confidence sets. These thresholds are illustrated via red and blue planes respectively and are obtained over the learning dataset. The panels on the bottom row of each example show the corresponding conformal confidence sets. Here the inner set is shown in red, plotted over the ground truth mask of the polyps, shown in yellow, plotted over the outer set which is shown in blue. The outer set contains the ground truth mask which contains the inner set in all examples. From these figures we see that the original scores provide tight inner confidence sets and the distance transformed scores instead provide tight outer confidence sets. The conclusion from the learning dataset is therefore that it makes sense to combine these two score transformations.

order to determine whether a polyps is present. Improved uncertainty quantification would require an improved segmentation model.

More precise results can be obtained at the expense of probabilistic guarantees, see Figures A14 and A15. A trade off must be made between precision and confidence. The most informative confidence level can be determined in advance based on the learning dataset and the desired type of coverage.

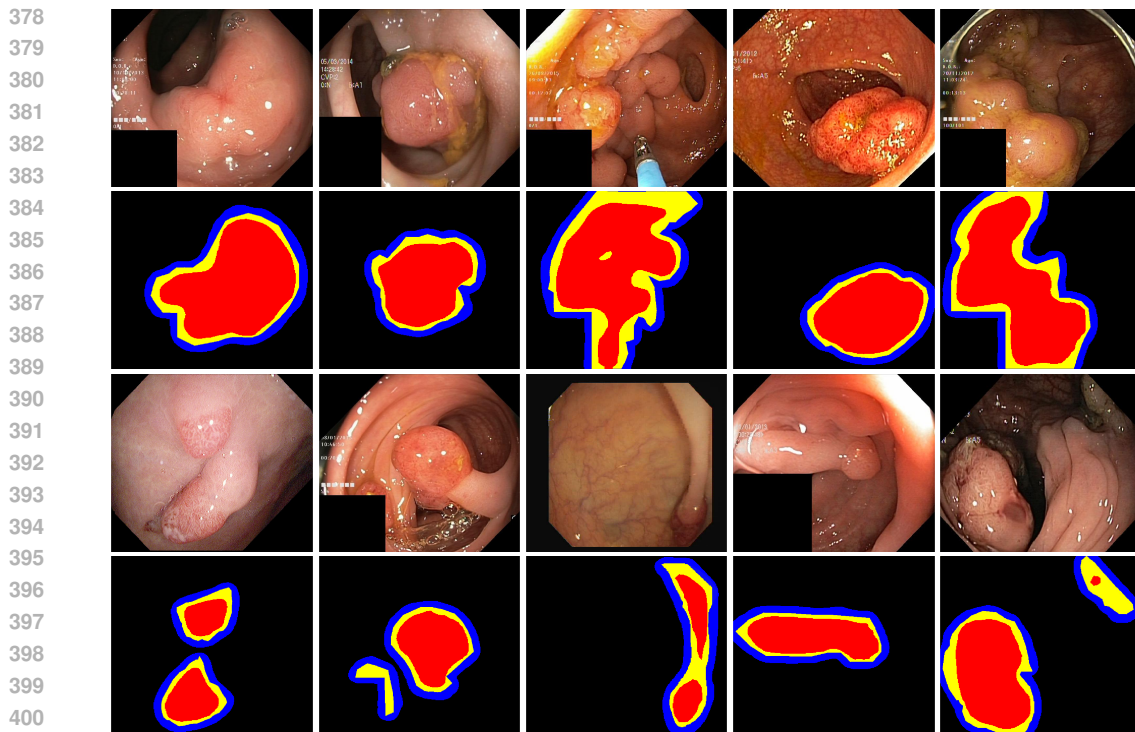


Figure 3: Conformal confidence sets for the polyps data. For each set of polyps images the top row shows the original endoscopic images with visible polyps and the second row presents the marginal 90% confidence sets, with ground truth masks shown in yellow. The inner sets and outer sets are shown in red and blue, obtained using the identity and distance transforms respectively. The figure shows the benefits of combining different score transformations for the inner and outer sets and illustrates the method’s effectiveness in accurately identifying polyp regions whilst providing informative spatial uncertainty bounds.

3.3 MEASURING THE COVERGE RATE

In this section we run validations to evaluate the false coverage rate of our approach. To do so we take the set aside 1500 images and run 1000 validations, in each validation dividing the data into 1000 calibration and 500 test images. In each division we calculate the conformal confidence sets using the different score transformations, based on thresholds derived from the calibration dataset, and evaluate the coverage rate on the test dataset. We average over all 1000 validations and present the results in Figure 4. Histograms for the 90% coverage obtained over all validation runs are shown in Figure A16.

From these results we can see that for all the approaches the coverage rate is controlled at or above the nominal level as desired. Using the bounding box scores results in slight over coverage at lower confidence levels. This is likely due to the discontinuities in the score functions b_I and b_O .

3.4 COMPARING THE EFFICIENCY OF THE BOUNDS

In this section we compare the efficiency of the confidence sets based on the different score transformations. To do so we run 1000 validations in each dividing and calibrating as in

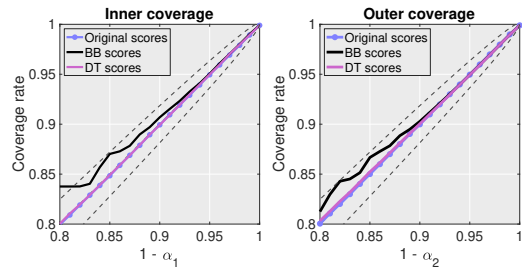
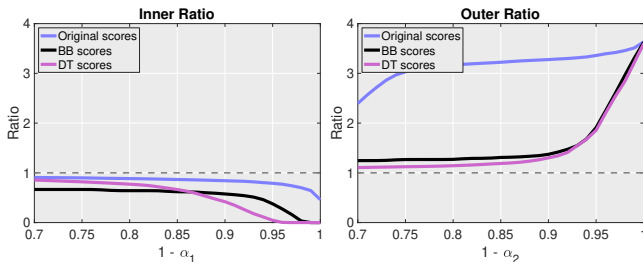


Figure 4: Coverage levels of the inner and outer sets averaged over 1000 validations for the original, distance transformed (DT) and bounding box (BB) scores.

432
433
434
435
436 Section 3.3. For each run we compute the ratio between the diameter of the inner set
437 and the diameter of the ground truth mask and average this ratio over the 500 test images.
438
439
440
441
442
443
444



445 Figure 5: Measuring the efficiency of the bound using the ratio
446 of the diameter of the coverage set to the diameter of the
447 true mask. The closer the ratio is to one the better. Higher
448 coverage rates lead to a lower efficiency. The original scores
449 provide the most efficient inner sets and the distance trans-
450 formed scores provide the most efficient outer sets.

4 APPLICATION TO BRAIN IMAGING SEGMENTATION

451
452
453
454
455
456 As a second application we consider
457 the task of skull stripping. This task
458 consists of segmenting the brain given
459 an Magnetic resonance image of a hu-
460 man head. For image segmentation
461 we use the HD-BET (Isensee et al.,
462 2019) neural network model which was
463 trained on dataset of 1,568 subjects and
464 has quickly become the defacto method
465 of performing brain mask segmen-
466 tation. In order to apply our methods
467 in this setting we combine data from
468 3 public datasets (LPBA40, NFBS, and
469 CC-359) resulting in 524 brain images
470 in total. This data is independent from
471 the data used to train HD-BET, see e.g.
472 (Isensee et al., 2019). We divide this data into 50 subjects to make up a learning dataset, use 300 subjects to perform calibration and use the remaining subjects for testing.

473 Based on the results of the learning dataset, see Appendix A.5.1, we see that the distance transformed
474 scores perform best for constructing both inner and outer confidence sets. The naive approach of
475 using the original scores perform very poorly for both inner and outer sets. Calibrating thresholds
476 for the distance transformed scores using the calibration dataset and applying to the images from
477 the testing dataset we obtain informative inner and outer confidence sets, as shown in Figure 6.
478 Validating as in Section XXX, we see that the false coverage rate is controlled to the nominal level,
479 see Section XXX.

5 APPLICATION TO TEETH SEGMENTATION

480
481
482
483 As a third application we consider the problem of teeth segmentation. We use a dataset (released
484 by Zhang et al. (2023)) consisting of scans of the teeth of 598 subjects and train a U-net based
485 GAN network using 400 subjects (following Hoshme (2024)). Divide the remaining 198 subjects into
170 to use as calibration data and 28 as a test dataset. We use the original training data as a

In order to make a smooth curve we average this quantity over all 1000 runs. A similar calculation is performed for the outer set. The results are shown in Figure 5. They show that the inner confidence sets produced by using the original scores are the most efficient. Instead, for the outer set, the distance transformed scores perform best. These results match the observations made on the learning dataset in Section 3.1 and the results found in Section 3.2.

We repeat this procedure instead targeting the proportion of the entire image which is under/over covered by the respective confidence sets. The results are shown in Figure A17 and can be interpreted similarly.

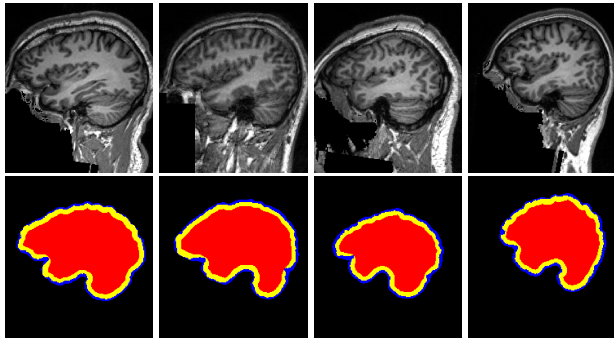


Figure 6: Inner and outer confidence sets for brain mask segmentation: both computed using the distance transformed scores. The true mask is shown in yellow.

learning dataset (note that this is independent of the calibration dataset so does not affect validity). We tried a variety of score transformations including distance transformations and smoothing, see Section A.6. Based on the learning data we chose the distance transformation for the outer sets and smoothing with a full width at half maximum of 2 pixels for the inner set. Calibrating thresholds on the calibration dataset and applying to the test data we obtain the results shown in Figure 7. Moreover, validating as in Section 3.3, we show that the false coverage rate is controlled to the nominal level in practice, see Section XXX.

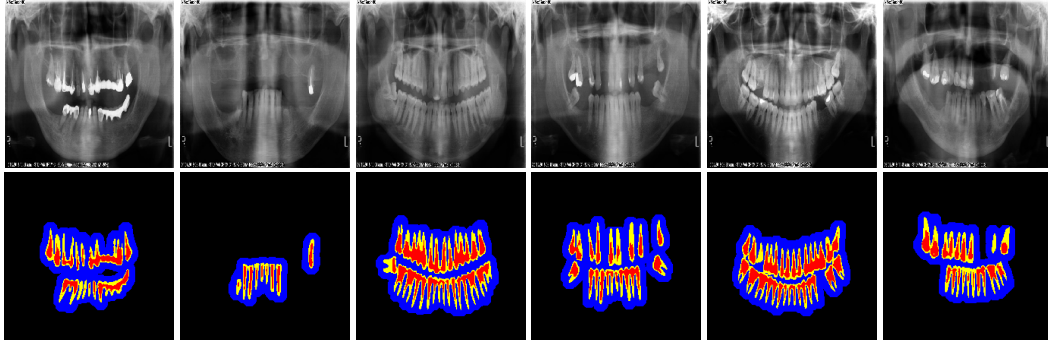


Figure 7: *Inner and outer confidence sets for brain mask segmentation computed using the original and distance transformed scores respectively. The true mask is shown in yellow.*

6 DISCUSSION

In this work, we have developed conformal confidence sets which offer probabilistic guarantees for the output of a black box image segmentation model and provide tight bounds. Our work helps to address the lack of formal uncertainty quantification in the application of deep neural networks to medical imaging which has limited the reliability and adoption of these models in practice. The use of improved neural networks which can better separate the scores within and outside the ground truth masks would lead to more precise confidence sets and optimizing this is an important area of research. We have here established validity guarantees and additionally showed that these can be used to theoretically justify a modified version of the max-additive bounding box based method of Andéol et al. (2023).

The use of the distance transformed scores was crucial in providing tight outer confidence bounds as the original neural network is by itself unable to reliably determine where the true masks end with certainty. The distance transformation penalizes regions away from the predicted mask, allowing the true mask to be distinguished from the background. In other datasets and model settings, other transformations may be appropriate. As such we strongly recommend the use of a learning dataset in order to calibrate the transformations and maximize precision of the resulting confidence bounds.

The confidence sets we develop in this paper are related in spirit to work on uncertainty quantification for spatial excursion sets (Chen et al. (2017), Bowring et al. (2019), Mejia et al. (2020)). These approaches instead assume that multiple observations from a signal plus noise model are observed and perform inference on the underlying signal rather than prediction. Unlike conformal inference these approaches rely on central limit theorems or distributional assumptions in order to provide spatial confidence regions with asymptotic coverage guarantees.

AVAILABILITY OF CODE

Matlab code to implement the methods of this paper and a demo on a downsampled version of the data is available in the supplementary material. The code is very fast: calculating inner and outer thresholds (over the 1000 images in the calibration set) requires approximately 0.03 seconds on the downsampled data on a standard laptop (Apple M3 chip with 16 GB RAM) and 2.64 seconds for the original dataset.

540 REFERENCES
541

- 542 Léo Andéol, Thomas Fel, Florence De Grancey, and Luca Mossina. Confident object detection
543 via conformal prediction and conformal risk control: an application to railway signaling. In
544 *Conformal and Probabilistic Prediction with Applications*, pp. 36–55. PMLR, 2023.
- 545 Anastasios N Angelopoulos and Stephen Bates. A gentle introduction to conformal prediction and
546 distribution-free uncertainty quantification. *arXiv preprint arXiv:2107.07511*, 2021.
547
- 548 Anastasios N Angelopoulos, Stephen Bates, Emmanuel J Candès, Michael I Jordan, and Lihua
549 Lei. Learn then test: Calibrating predictive algorithms to achieve risk control. *arXiv preprint
550 arXiv:2110.01052*, 2021.
- 551 Anastasios N. Angelopoulos, Stephen Bates, Adam Fisch, Lihua Lei, and Tal Schuster. Conformal
552 risk control. In *Proceedings of the International Conference on Learning Representations (ICLR)*,
553 2024.
- 554 Stephen Bates, Anastasios Angelopoulos, Lihua Lei, Jitendra Malik, and Michael Jordan.
555 Distribution-free, risk-controlling prediction sets. *Journal of the ACM (JACM)*, 68(6):1–34, 2021.
556
- 557 Yoav Benjamini and Yosef Hochberg. Controlling the false discovery rate: a practical and powerful
558 approach to multiple testing. *Journal of the Royal statistical society: series B (Methodological)*,
559 57(1):289–300, 1995.
560
- 561 Jorge Bernal, Javier Sánchez, and Fernando Vilarino. Towards automatic polyp detection with a
562 polyp appearance model. *Pattern Recognition*, 45(9):3166–3182, 2012.
- 563 Gilles Blanchard, Guillermo Durand, Ariane Marandon-Carlhian, and Romain Périer. Fdr control
564 and fdp bounds for conformal link prediction. *arXiv preprint arXiv:2404.02542*, 2024.
565
- 566 Gunilla Borgefors. Distance transformations in digital images. *Computer vision, graphics, and
567 image processing*, 34(3):344–371, 1986.
- 568 Hanna Borgli, Vajira Thambawita, Pia H Smedsrud, Steven Hicks, Debesh Jha, Sigrun L Eskeland,
569 Kristin Ranheim Randel, Konstantin Pogorelov, Mathias Lux, Duc Tien Dang Nguyen, et al.
570 Hyperkvasir, a comprehensive multi-class image and video dataset for gastrointestinal endoscopy.
571 *Scientific data*, 7(1):283, 2020.
572
- 573 Alexander Bowring, Fabian Telschow, Armin Schwartzman, and Thomas E. Nichols. Spatial confi-
574 dence sets for raw effect size images. *NeuroImage*, 203:116187, 2019.
- 575 Yen-Chi Chen, Christopher R Genovese, and Larry Wasserman. Density level sets: Asymptotics,
576 inference, and visualization. *Journal of the American Statistical Association*, 112(520):1684–
577 1696, 2017.
578
- 579 Florence de Grancey, Jean-Luc Adam, Lucian Alecu, Sébastien Gerchinovitz, Franck Mamalet, and
580 David Vigouroux. Object detection with probabilistic guarantees. In *Fifth International Workshop
581 on Artificial Intelligence Safety Engineering (WAISE 2022)*, 2022.
- 582 Deng-Ping Fan, Ge-Peng Ji, Tao Zhou, Geng Chen, Huazhu Fu, Jianbing Shen, and Ling Shao.
583 Pranet: Parallel reverse attention network for polyp segmentation. In *International conference on
584 medical image computing and computer-assisted intervention*, pp. 263–273. Springer, 2020.
585
- 586 Chuan Guo, Geoff Pleiss, Yu Sun, and Kilian Q Weinberger. On calibration of modern neural
587 networks. In *International conference on machine learning*, pp. 1321–1330. PMLR, 2017.
- 588 Chirag Gupta, Aleksandr Podkopaev, and Aaditya Ramdas. Distribution-free binary classification:
589 prediction sets, confidence intervals and calibration. *Advances in Neural Information Processing
590 Systems*, 33:3711–3723, 2020.
591
- 592 Kaled Hoshme. Adult tooth segmentation using u-net based gan. <https://www.kaggle.com/code/kaledhoshme/adult-tooth-segmentation-u-net-based-gan/>,
593 2024. Accessed: 2024-11-17.

- 594 Fabian Isensee, Marianne Schell, Irada Pflueger, Gianluca Brugnara, David Bonekamp, Ulf Neu-
 595 berger, Antje Wick, Heinz-Peter Schlemmer, Sabine Heiland, Wolfgang Wick, et al. Automated
 596 brain extraction of multisequence mri using artificial neural networks. *Human brain mapping*, 40
 597 (17):4952–4964, 2019.
- 598 Seyed Ali Jalalifar, Hany Soliman, Arjun Sahgal, and Ali Sadeghi-Naini. Impact of tumour seg-
 599 mentation accuracy on efficacy of quantitative mri biomarkers of radiotherapy outcome in brain
 600 metastasis. *Cancers*, 14(20):5133, 2022.
- 602 Alain Jungo, Fabian Balsiger, and Mauricio Reyes. Analyzing the quality and challenges of uncer-
 603 tainty estimations for brain tumor segmentation. *Frontiers in neuroscience*, 14:282, 2020.
- 604 Carsten Maple. Geometric design and space planning using the marching squares and marching
 605 cube algorithms. In *2003 international conference on geometric modeling and graphics, 2003.*
 606 Proceedings
- 607 pp. 90–95. IEEE, 2003.
- 608 Ariane Marandon. Conformal link prediction for false discovery rate control. *TEST*, pp. 1–22, 2024.
- 609
- 610 Amanda F Mejia, Yu Yue, David Bolin, Finn Lindgren, and Martin A Lindquist. A bayesian general
 611 linear modeling approach to cortical surface fmri data analysis. *Journal of the American Statistical
 612 Association*, 115(530):501–520, 2020.
- 613 Luca Mossina, Joseba Dalmau, and Léo Andéol. Conformal semantic image segmentation: Post-
 614 hoc quantification of predictive uncertainty. In *Proceedings of the IEEE/CVF Conference on
 615 Computer Vision and Pattern Recognition*, pp. 3574–3584, 2024.
- 616
- 617 Bruce Cyusa Mukama, Soundouss Messoudi, Sylvain Rousseau, and Sébastien Destercke. Copula-
 618 based conformal prediction for object detection: a more efficient approach. *Proceedings of Ma-
 619 chine Learning Research*, 230:1–18, 2024.
- 620 Harris Papadopoulos, Kostas Proedrou, Volodya Vovk, and Alex Gammerman. Inductive confidence
 621 machines for regression. In *Machine learning: ECML 2002: 13th European conference on ma-
 622 chine learning Helsinki, Finland, August 19–23, 2002 proceedings 13*, pp. 345–356. Springer,
 623 2002.
- 624
- 625 Edward F Patz, Paul Pinsky, Constantine Gatsonis, JoRean D Sicks, Barnett S Kramer, Mar-
 626 tin C Tammemägi, Caroline Chiles, William C Black, Denise R Aberle, NLST Overdiagnosis
 627 Manuscript Writing Team, et al. Overdiagnosis in low-dose computed tomography screening for
 628 lung cancer. *JAMA internal medicine*, 174(2):269–274, 2014.
- 629
- 630 Konstantin Pogorelov, Kristin Ranheim Randel, Carsten Griwodz, Sigrun Losada Eskeland, Thomas
 631 de Lange, Dag Johansen, Concetto Spampinato, Duc-Tien Dang-Nguyen, Mathias Lux, Pe-
 632 ter Thelin Schmidt, Michael Riegler, and Pål Halvorsen. Kvasir: A multi-class image dataset
 633 for computer aided gastrointestinal disease detection. In *Proceedings of the 8th ACM on Multi-
 634 media Systems Conference, MMSys’17*, pp. 164–169, New York, NY, USA, 2017. ACM. ISBN
 978-1-4503-5002-0. doi: 10.1145/3083187.3083212.
- 635
- 636 Glenn Shafer and Vladimir Vovk. A tutorial on conformal prediction. *Journal of Machine Learning
 637 Research*, 9(3), 2008.
- 638
- 639 Juan Silva, Aymeric Histace, Olivier Romain, Xavier Dray, and Bertrand Granado. Toward em-
 640 bedded detection of polyps in wce images for early diagnosis of colorectal cancer. *International
 641 journal of computer assisted radiology and surgery*, 9:283–293, 2014.
- 642
- 643 Sophia Sun and Rose Yu. Copula conformal prediction for multi-step time series forecasting. In
 644 *International Conference on Learning Representations (ICLR)*, 2024.
- 645
- 646 Ryan J Tibshirani, Rina Foygel Barber, Emmanuel Candes, and Aaditya Ramdas. Conformal pre-
 647 diction under covariate shift. *Advances in neural information processing systems*, 32, 2019.
- 648
- 649 Eric J Topol. High-performance medicine: the convergence of human and artificial intelligence.
 650 *Nature medicine*, 25(1):44–56, 2019.

648 Vladimir Vovk, Alexander Gammerman, and Glenn Shafer. *Algorithmic learning in a random world*,
649 volume 29. Springer, 2005.
650

651 Håkan Wieslander, Philip J Harrison, Gabriel Skogberg, Sonya Jackson, Markus Fridén, Johan
652 Karlsson, Ola Spjuth, and Carolina Wählby. Deep learning with conformal prediction for hi-
653 erarchical analysis of large-scale whole-slide tissue images. *IEEE journal of biomedical and*
654 *health informatics*, 25(2):371–380, 2020.

655 Keith J. Worsley, Alan C Evans, Sean Marrett, and P Neelin. A three-dimensional statistical analysis
656 for CBF activation studies in human brain. *JCBFM*, 1992.
657

658 Yifan Zhang, Fan Ye, Lingxiao Chen, Feng Xu, Xiaodiao Chen, Hongkun Wu, Mingguo Cao, Yunx-
659 iang Li, Yaqi Wang, and Xingru Huang. Children’s dental panoramic radiographs dataset for
660 caries segmentation and dental disease detection. *Scientific Data*, 10(1):380, 2023.
661
662
663
664
665
666
667
668
669
670
671
672
673
674
675
676
677
678
679
680
681
682
683
684
685
686
687
688
689
690
691
692
693
694
695
696
697
698
699
700
701

702 **A APPENDIX**

704 **A.1 OBTAINING CONFORMAL CONFIDENCE SETS WITH INCREASING COMBINATION**
 705 **FUNCTIONS**

707 As discussed in Remark 2.3 the results of Sections 2.2 and 2.3 can be generalized to a wider class
 708 of combination functions.

709 **Definition A.1.** We define a suitable combination function to be a function $C : \mathcal{P}(\mathcal{V}) \times \mathcal{X} \rightarrow \mathbb{R}$
 710 which is increasing in the sense that for all sets $\mathcal{A} \subseteq \mathcal{V}$ and each $v \in \mathcal{A}$, $C(v, X) \leq C(\mathcal{A}, X)$ for
 711 all $X \in \mathcal{X}$.

712 The maximum is a suitable combination function since $X(v) = \max_{v \in \{v\}} X(v) \leq \max_{v \in \mathcal{A}} X(v)$.
 713 As such this framework directly generalizes the results of the main text.

714 We can construct generalized marginal confidence sets as follows.

715 **Theorem A.2.** (*Marginal inner set*) Under Assumptions 1 and 2, given $\alpha_1 \in (0, 1)$, define

$$717 \quad \lambda_I(\alpha_1) = \inf \left\{ \lambda : \frac{1}{n} \sum_{i=1}^n 1 [C(\{v \in \mathcal{V} : Y_i(v) = 1\}, f_I(s(X_i))) \leq \lambda] \geq \frac{\lceil (1 - \alpha_1)(n + 1) \rceil}{n} \right\},$$

720 for a suitable combination function C , and define $I(X) = \{v \in \mathcal{V} : C(v, f_I(s(X))) > \lambda_I(\alpha_1)\}$.
 721 Then,

$$722 \quad \mathbb{P}(I(X_{n+1}) \subseteq \{v \in \mathcal{V} : Y_{n+1}(v) = 1\}) \geq 1 - \alpha_1. \quad (7)$$

723 The proof follows that of Theorem 2.1. The key observation is that for any suitable combination
 724 function C , given $\lambda \in \mathbb{R}$, $\mathcal{A} \subseteq \mathcal{V}$ and $X \in \mathcal{X}$, $C(\mathcal{A}, X) \leq \lambda$ implies that $C(v, X) \leq \lambda$. This is the
 725 relevant property of the maximum which we used for the results in the main text. For the outer set
 726 we similarly have the following.

727 **Theorem A.3.** (*Marginal outer set*) Under Assumptions 1 and 2, given $\alpha_2 \in (0, 1)$, define

$$728 \quad \lambda_O(\alpha_2) = \inf \left\{ \lambda : \frac{1}{n} \sum_{i=1}^n 1 [C(\{v \in \mathcal{V} : Y_i(v) = 0\}, -f_O(s(X_i))) \leq \lambda] \geq \frac{\lceil (1 - \alpha_2)(n + 1) \rceil}{n} \right\}.$$

731 for a suitable combination function C , and let $O(X) = \{v \in \mathcal{V} : C(v, -f_O(s(X))) \leq \lambda_O(\alpha_2)\}$.
 732 Then,

$$733 \quad \mathbb{P}(\{v \in \mathcal{V} : Y_{n+1}(v) = 1\} \subseteq O(X_{n+1})) \geq 1 - \alpha_2. \quad (8)$$

734 Joint results can be analogously obtained.

736 **A.2 OBTAINING CONFIDENCE SETS FROM RISK CONTROL**

738 We can alternatively establish Theorems 2.1 and A.2 using an argument from risk control (Angelopoulos et al., 2024). In particular, given an image pair (X, Y) and $\lambda \in \mathbb{R}$, let

$$740 \quad I_\lambda(X) = \{v \in \mathcal{V} : f_I(s(X), v) > \lambda\}.$$

741 Define a loss function, $L : \mathcal{P}(\mathcal{V}) \times \mathcal{Y} \rightarrow \mathbb{R}$ which sends (X, Y) to

$$742 \quad L(I_\lambda(X), Y) = 1 [I_\lambda(X) \not\subseteq \{v \in \mathcal{V} : Y(v) = 1\}].$$

743 For $i = 1, \dots, n + 1$, let $L_i(\lambda) = L(I_\lambda(X_i), Y_i)$. Arguing as in the proof of Theorem 2.1 it follows
 744 that $L_i(\lambda) = 1[\tau_i > \lambda]$. Then applying Theorem 1 of Angelopoulos et al. (2024) it follows that

$$745 \quad \mathbb{E}[L_{n+1}(\hat{\lambda})] \leq \alpha_1,$$

747 where $\hat{\lambda} = \inf \left\{ \lambda : \frac{1}{n} \sum_{i=1}^n L_i(\lambda) \leq \alpha_1 - \frac{1 - \alpha_1}{n} \right\}$. Arguing as in Appendix A of (Angelopoulos
 748 et al., 2024) it follows that

$$749 \quad \hat{\lambda} = \inf \left\{ \lambda : \frac{1}{n} \sum_{i=1}^n 1 [\tau_i \leq \lambda] \geq \frac{\lceil (1 - \alpha_1)(n + 1) \rceil}{n} \right\} = \lambda_I(\alpha_1),$$

752 and so $I(X) = I_{\hat{\lambda}}(X)$. As such

$$753 \quad \mathbb{P}(I(X_{n+1}) \subseteq \{v \in \mathcal{V} : Y_{n+1}(v) = 1\}) = 1 - \mathbb{E}[L_{n+1}(\hat{\lambda})] \geq 1 - \alpha_1, \quad (9)$$

754 and we recover the desired result. Arguing similarly it is possible to establish a proof of Theorem
 755 2.2.

756 A.3 DERIVING CONFIDENCE SETS FROM BOUNDING BOXES
 757

758 We can use our results in order to provide valid inference for bounding boxes via an adaption of the
 759 approach of Andéol et al. (2023). In particular given $Z \in \mathcal{Y}$, let $B_{I,\max}(Z)$ be the largest box which
 760 can be contained within the set $\{v \in \mathcal{V} : Z(v) = 1\}$ and let $B_{O,\min}(Z)$ be the smallest box which
 761 contains the set $\{v \in \mathcal{V} : Z(v) = 1\}$. Given $Y \in \mathcal{Y}$, let $cc(Y) \subseteq \mathcal{P}(\mathcal{V})$ denote the set of connected
 762 components of the set $\{v \in \mathcal{V} : Y(v) = 1\}$ for a given connectivity criterion (which we take to be
 763 4 in our examples), and note that these components can themselves be identified as elements of \mathcal{Y} .
 764 Define

$$765 \quad B_I(Y) = \cup_{c \in cc(Y)} B_{I,\max}(c) \text{ and } B_O(Y) = \cup_{c \in cc(Y)} B_{O,\min}(c)$$

766 to be the unions of the largest inner and smallest outer boxes of the connected components of the
 767 image Y , respectively. Then define

$$768 \quad \hat{B}_I(s(X)) = \cup_{c \in cc(\hat{M}(X))} B_{I,\max}(c) \text{ and } \hat{B}_O(s(X)) = \cup_{c \in cc(\hat{M}(X))} B_{O,\min}(c)$$

770 to be the unions of the largest inner and smallest outer boxes of the connected components of the
 771 predicted mask $\hat{M}(X)$, respectively. Note that this is well-defined as $\hat{M}(X)$ is a function of $s(X)$.

772 For the remainder of this section we shall assume that $\mathcal{V} \subset \mathbb{R}^2$, this is not strictly necessary but
 773 will help to simplify notation. Given $u, v \in \mathcal{V}$, write $u = (u_1, u_2)$ and $v = (v_1, v_2)$ and let
 774 $\rho(u, v) = \max(|u_1 - v_1|, |u_2 - v_2|)$ be the chessboard metric.

775 **Definition A.4.** (Bounding box scores) For each $X \in \mathcal{X}$ and $v \in \mathcal{V}$, let

$$777 \quad b_I(s(X), v) = d_\rho(\hat{B}_I(s(X)), v) \text{ and } b_O(s(X), v) = d_\rho(\hat{B}_O(s(X)), v)$$

779 be the distance transformed scores based on the chessboard distance to the predicted inner and outer
 780 box collections $\hat{B}_I(s(X))$ and $\hat{B}_O(s(X))$, respectively. We also define a combination of these b_M ,
 781 primarily for the purposes of plotting in Figure 2, as follows. Let $b_M(s(X), v) = b_O(s(X), v)$ for
 782 each $v \notin \hat{B}_O(s(X))$ and let $b_M(s(X), v) = \max(b_I(s(X), v), 0)$ for $v \in \hat{B}_O(s(X))$. We shall
 783 write $b_I(s(X)) \in \mathcal{X}$ to denote the image which has $b_I(s(X))(v) = b_I(s(X), v)$ and similarly for
 784 $b_O(s(X))$ and $b_M(s(X))$.

785 Now consider the sequences of image pairs $(X_i, B_i^I)_{i=1}^n$ and $(X_i, B_i^O)_{i=1}^n$. These both satisfy ex-
 786 changeability and so, applying Theorems A.2 and A.3, we obtain the following bounding box valid-
 787 ity results.

788 **Corollary A.5. (Marginal inner bounding boxes)** Suppose Assumption 1 holds and that $(X_i, Y_i)_{i=1}^{n+1}$
 789 is independent of the functions s and b_I . Given $\alpha_1 \in (0, 1)$, define

$$791 \quad \lambda_I(\alpha_1) = \inf \left\{ \lambda : \frac{1}{n} \sum_{i=1}^n 1 [C(B_i^I, b_I(s(X_i))) \leq \lambda] \geq \frac{\lceil (1 - \alpha_1)(n + 1) \rceil}{n} \right\}, \quad (10)$$

794 for a suitable combination function C , and define $I(X) = \{v \in \mathcal{V} : C(v, b_I(s(X))) > \lambda_I(\alpha_1)\}$.
 795 Then,

$$796 \quad \mathbb{P}(I(X_{n+1}) \subseteq B_{n+1}^I \subseteq \{v \in \mathcal{V} : Y_{n+1}(v) = 1\}) \geq 1 - \alpha_1.$$

797 **Corollary A.6. (Marginal outer bounding boxes)** Suppose Assumption 1 holds and that $(X_i, Y_i)_{i=1}^{n+1}$
 798 is independent of the functions s and b_O . Given $\alpha_2 \in (0, 1)$, define

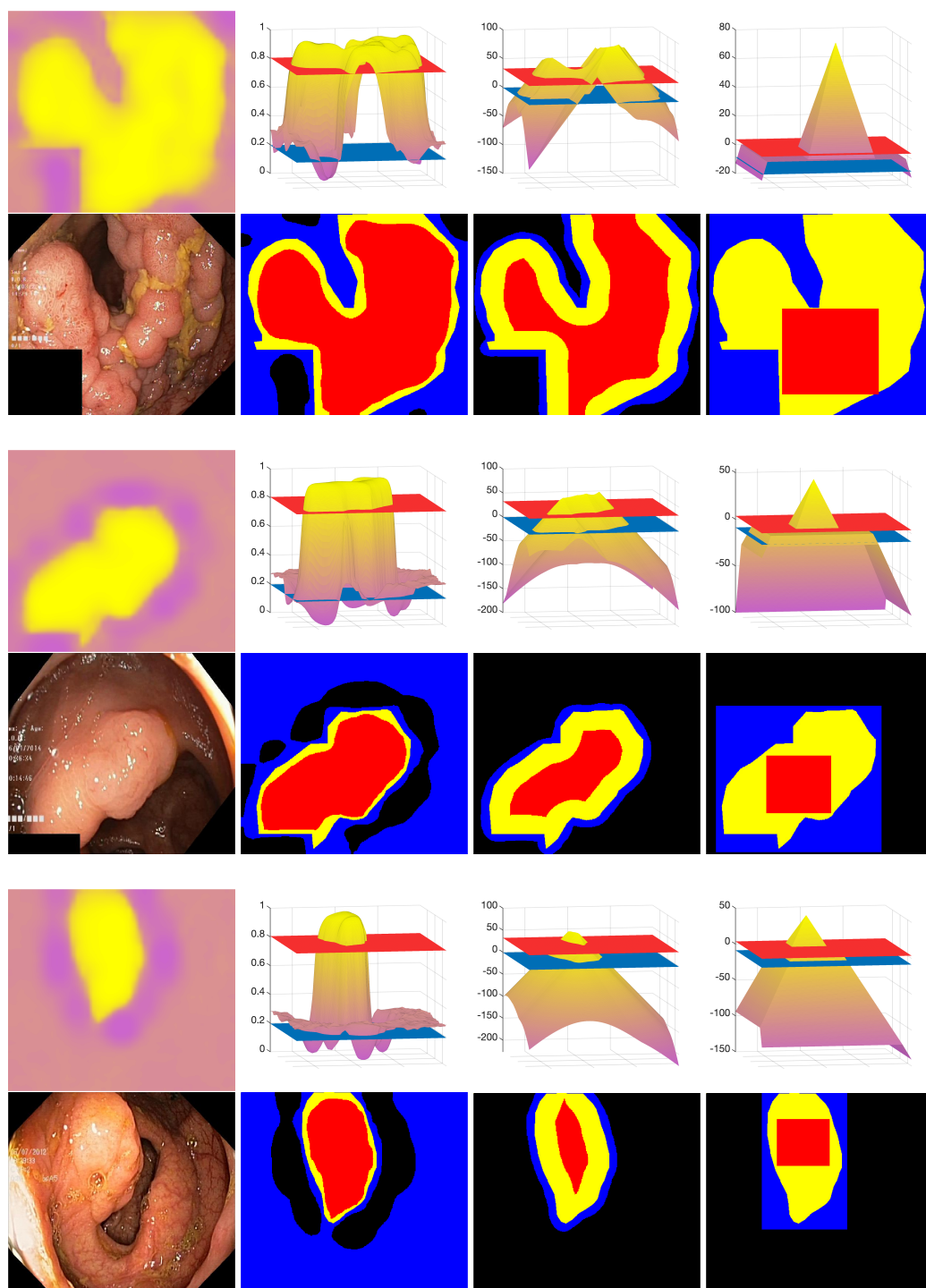
$$800 \quad \lambda_O(\alpha_2) = \inf \left\{ \lambda : \frac{1}{n} \sum_{i=1}^n 1 [C(B_i^O, -b_O(s(X_i))) \leq \lambda] \geq \frac{\lceil (1 - \alpha_2)(n + 1) \rceil}{n} \right\}. \quad (11)$$

803 for a suitable combination function C , and let $O(X) = \{v \in \mathcal{V} : C(v, -b_O(s(X))) \leq \lambda_O(\alpha_2)\}$.
 804 Then,

$$805 \quad \mathbb{P}(\{v \in \mathcal{V} : Y_{n+1}(v) = 1\} \subseteq B_{n+1}^O \subseteq O(X_{n+1})) \geq 1 - \alpha_2.$$

806 Joint results can be obtained in a similar manner to those in Section 2.3.
 807

808
 809

810 A.4 ADDITIONAL SETTINGS FOR POLYPS SEGMENTATION
811812 A.4.1 ADDITIONAL EXAMPLES FROM THE LEARNING DATASET
813860 Figure A8: Additional examples from the learning dataset. The layout of these figures is the same
861 as for Figure 2.
862
863

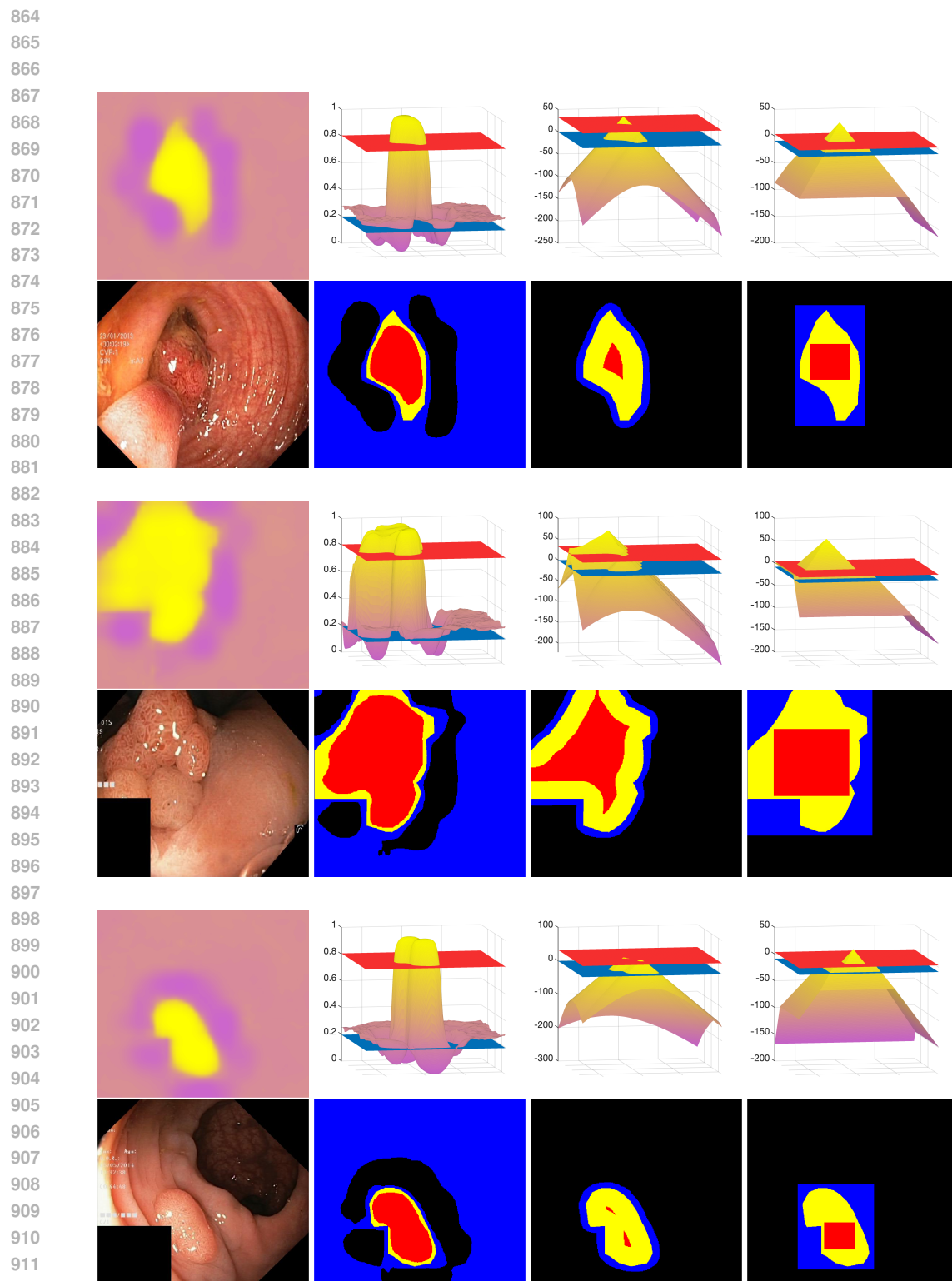
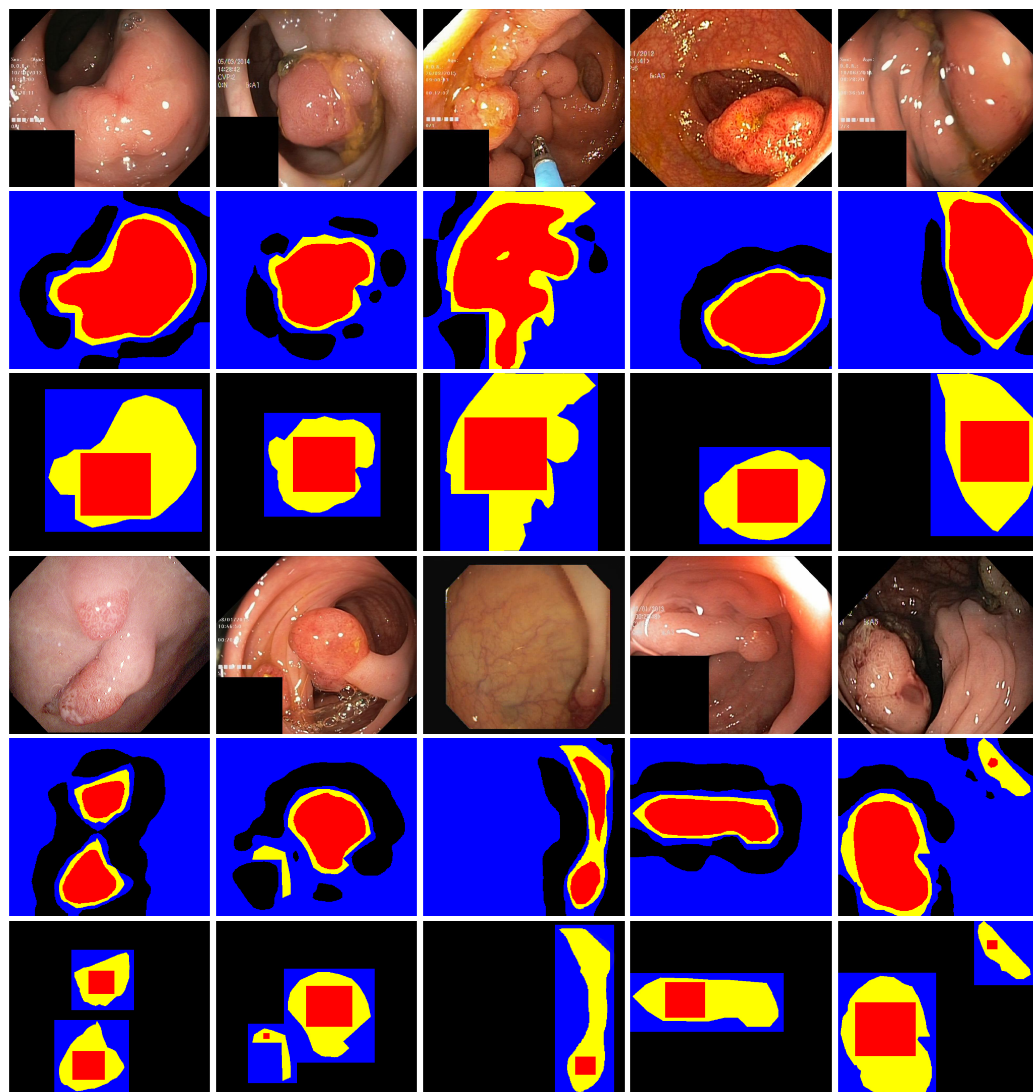
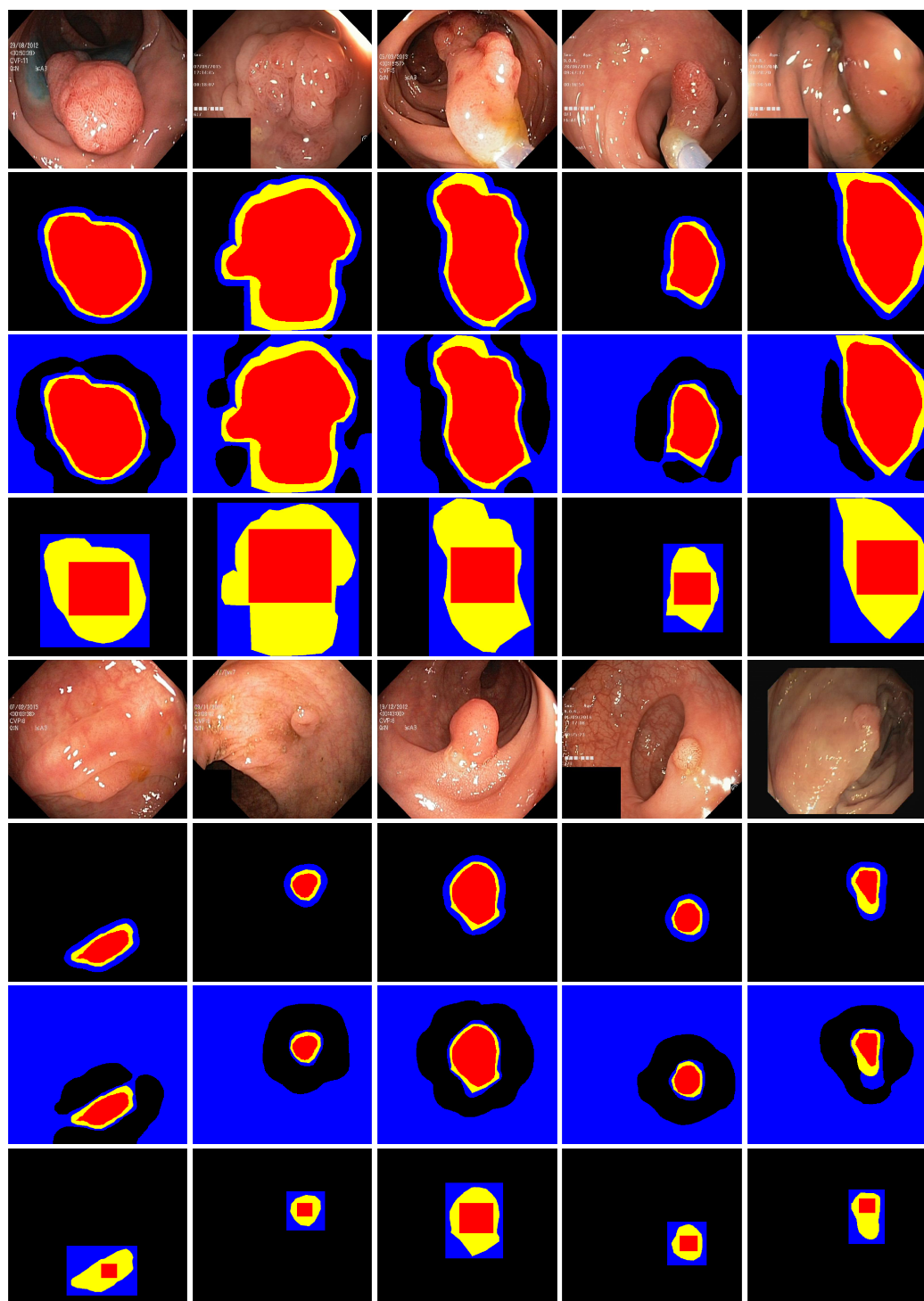


Figure A9: Futher examples from the learning dataset. The layout of these figures is the same as for Figure 2.

918 A.4.2 VALIDATION FIGURES FOR THE ORIGINAL AND BOUNDING BOX SCORES
919

956 Figure A10: Conformal confidence sets for the polyps data examples from Figure 3 for alternative
957 scores. In each set of panels the confidence obtained from using the original scores are shown in
958 the middle row and those obtained from the bounding box scores are shown in the bottom row. As
959 observed on the learning dataset the outer sets obtained when using the original scores are very large
960 and uninformative.

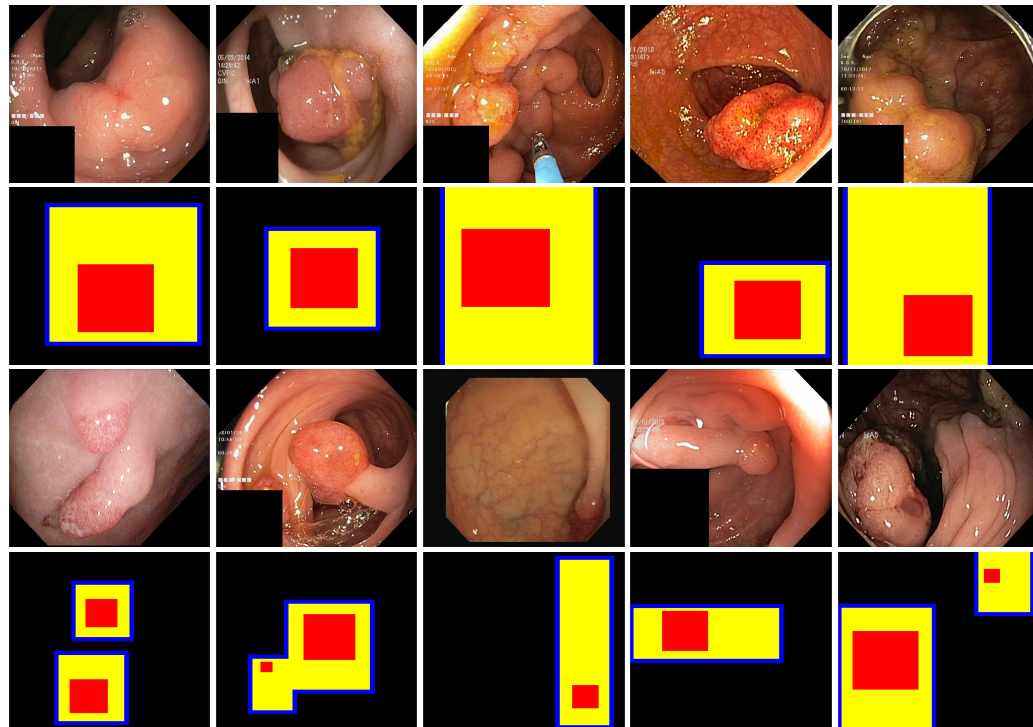
961
962
963
964
965
966
967
968
969
970
971

972 A.4.3 ADDITIONAL VALIDATION FIGURES
973

974
975
976
977
978
979
980
981
982
983
984
985
986
987
988
989
990
991
992
993
994
995
996
997
998
999
1000
1001
1002
1003
1004
1005
1006
1007
1008
1009
1010
1011
1012
1013
1014
1015
1016
1017
1018
1019
1020
1021
1022
1023
1024
1025

Figure A11: Additional validation examples. In each example, after the original images, the rows are (from top to bottom) the combination of the original and distance transformed scores, then the original scores and finally the bounding box scores.

1026 A.4.4 CONFIDENCE SETS FOR THE BOUNDING BOXES
 1027



1028
 1029
 1030
 1031
 1032
 1033
 1034
 1035
 1036
 1037
 1038
 1039
 1040
 1041
 1042
 1043
 1044
 1045
 1046
 1047
 1048
 1049
 1050
 1051
 1052
 1053
 1054
 1055
 1056
 1057
 1058
 1059
 1060
 1061
 1062
 1063
 1064
 1065
 1066
 1067
 1068
 1069
 1070
 1071
 1072
 1073
 1074
 1075
 1076
 1077
 1078
 1079

Figure A12: Conformal confidence sets for the boundary boxes themselves using the approach introduced in Section A.3. The ground truth outer bounding boxes are shown in yellow.

A.4.5 JOINT 90% CONFIDENCE REGIONS

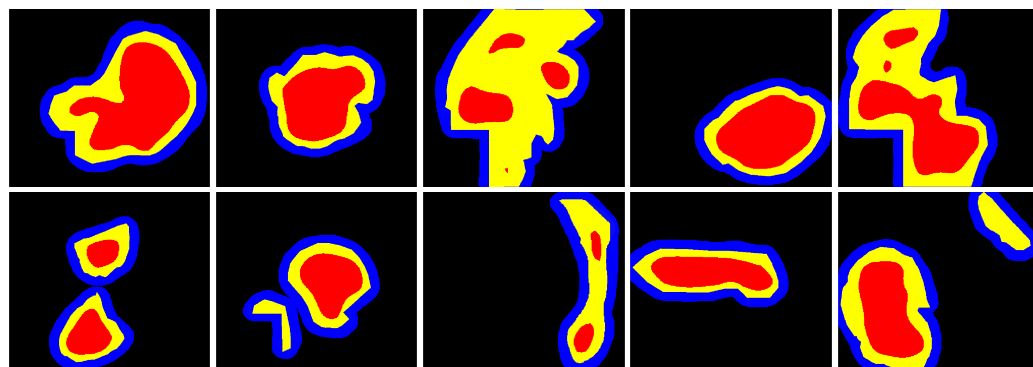
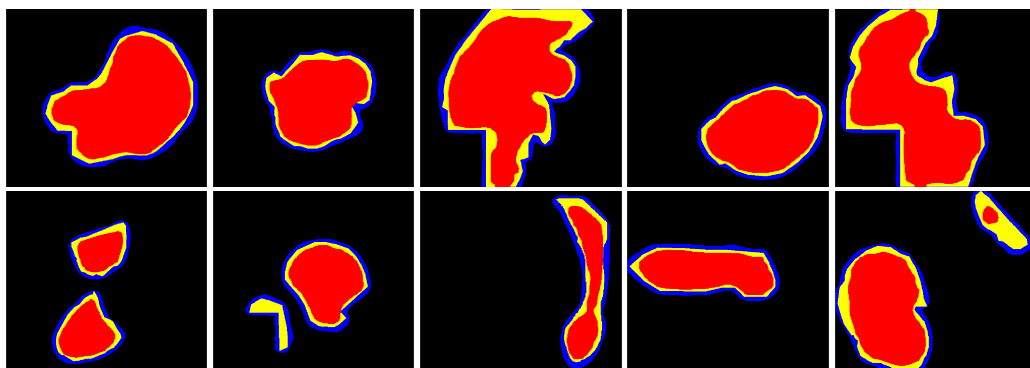
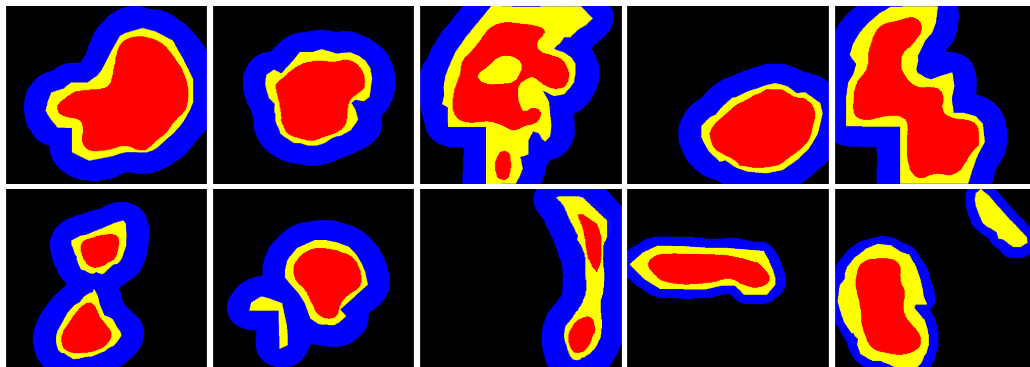
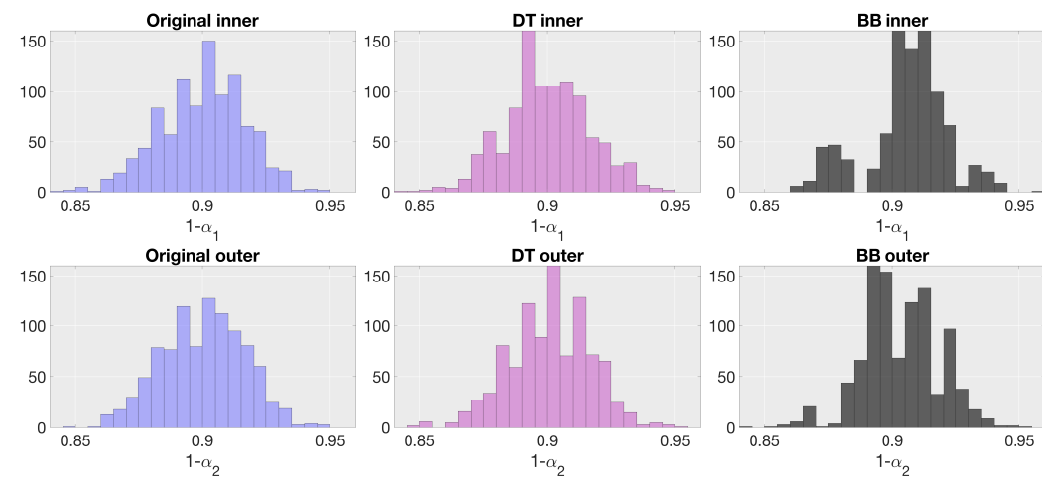


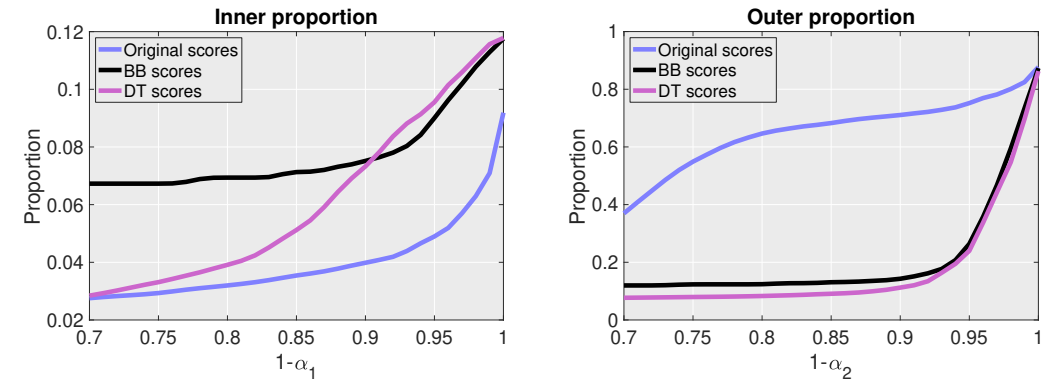
Figure A13: Joint 90% conformal confidence sets obtained using Corollary 2.5, with $\alpha_1 = 0.02$ and $\alpha_2 = 0.08$, for the polyps images in Figure 3.

1080 A.4.6 MARGINAL 80 % CONFIDENCE REGIONS
10811094
1095 Figure A14: Marginal 80% conformal confidence sets obtained for the polyps images in Figure 3.
1096
10971098 A.4.7 MARGINAL 95 % CONFIDENCE REGIONS
10991112
1113 Figure A15: Marginal 95% conformal confidence sets obtained using for the polyps images in Figure
1114 3. These sets are also joint 90% confidence sets with equally weighted $\alpha_1 = \alpha_2 = 0.05$. The
1115 influence of the weighting scheme can therefore examined by comparing to Figure A13.
1116
1117
1118
1119
1120
1121
1122
1123
1124
1125
1126
1127
1128
1129
1130
1131
1132
1133

21

1134 A.4.8 HISTOGRAMS OF THE COVERAGE
1135

1152 Figure A16: Histograms of the coverage rates obtained across each of the validation resamples for
1153 90% inner and outer marginal confidence sets. We plot the results for the original scores, distance
1154 transformed scores (DT) and boundary box scores (BB) from left to right. The bounding box scores
1155 are discontinuous which is the cause of the discreteness of the rightmost histograms.
1156

1157 A.4.9 COMPARING THE PROPORTION
1158

1172 Figure A17: Measuring the proportion of the entire image which is under/over covered by the
1173 respective confidence sets. Left: proportion of the image which lies within the true mask but outside
1174 of the inner set. Right: proportion of the image which lies within the confidence set but outside of
1175 the true mask. For both a lower proportion corresponds to increased precision.
1176
1177
1178
1179
1180
1181
1182
1183
1184
1185
1186
1187

1188
1189

A.5 ADDITIONAL SETTINGS FOR BRAIN MASK SEGMENTATION

1190
1191A.5.1 COMPARING ORIGINAL AND DISTANCE TRANSFORMED SCORES ON THE LEARNING
1192 DATASET

1193

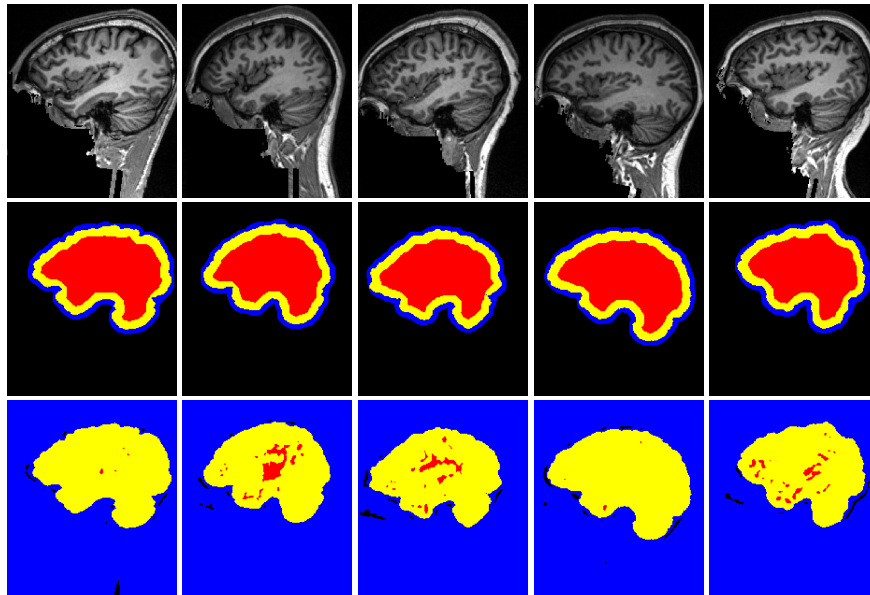
1194
1195
1196
1197
1198
1199
1200
1201
1202
1203
1204
1205
1206
1207
1208
1209
1210
1211
1212

Figure A18: *Learning the best transformation for brain mask segmentation. First row: original images from different subjects. Second row: confidence sets provided by calibrating the distance transformed scores on the learning dataset. Third row: confidence sets produced using the original scores on the learning dataset. Using the original scores produced very bad results. Instead the distance transformation is a big improvement. Note that the improvement obtained by using the distance scores is even more when using the full calibration data, see Figure 6. This is because the learning dataset is relatively small and does not capture the full picture. The results at test time for the original scores are equally bad as for the learning data, see Figure A20.*

1221
1222
1223
1224
1225
1226
1227
1228
1229
1230
1231
1232
1233
1234
1235
1236
1237
1238
1239
1240
1241

1242
1243

A.5.2 COMPARING SMOOTH TRANSFORMED SCORES ON THE LEARNING DATASET

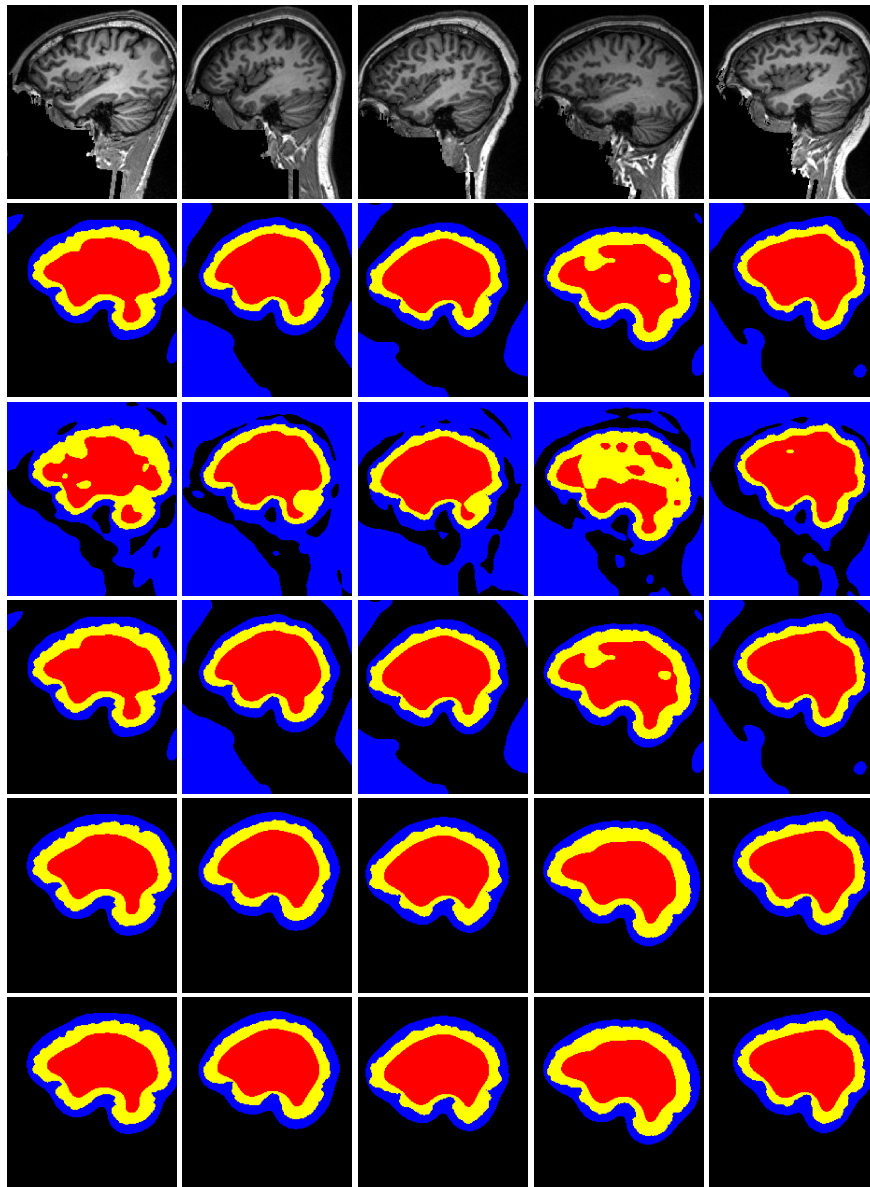
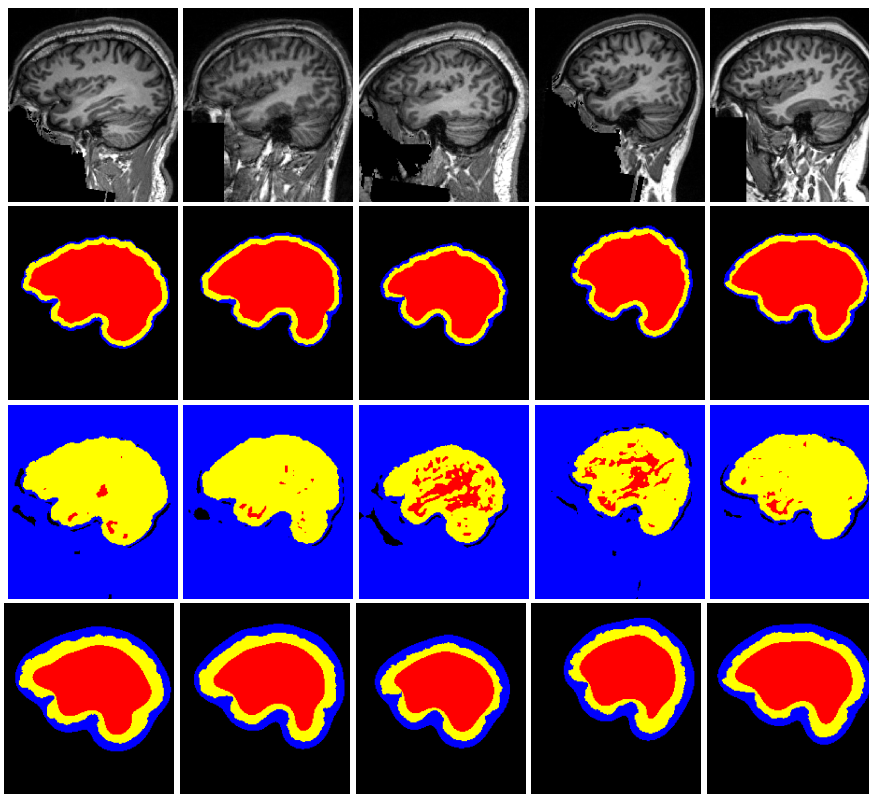
1244
1245
1246
1247
1248
1249
1250
1251
1252
1253
1254
1255
1256
1257
1258
1259
1260
1261
1262
1263
1264
1265
1266
1267
1268
1269
1270
1271
1272
1273
1274
1275
1276
1277
1278
1279
1280
1281
12821283
1284
1285
1286
1287
1288
1289
1290
1291
1292
1293
1294
1295

Figure A19: *Inner and outer sets computed by comparing smooth score transformations on the learning dataset. Scores were smoothed using a Gaussian kernel with full width at half maximum (FWHM) taking values in $\{5, 10, 15, 20, 25\}$ mm. The resulting inner and outer sets based on increasing levels of applied smoothness are shown from top to bottom. The performance appears to peak at 20mm.*

1296 A.5.3 COMPARING ORIGINAL AND DISTANCE TRANSFORMED SCORES ON THE TEST
 1297 DATASET
 1298



1324 Figure A20: *Inner and outer confidence sets for brain mask segmentation using the distance trans-*
 1325 *formed and original scores. Top row: brain images for each subject. 2nd row: the inner and outer*
 1326 *confidence sets produced by calibrating the distance transformed scores on the calibration dataset.*
 1327 *3rd row: the inner and outer confidence sets produced by calibrating the original scores on the cal-*
 1328 *ibration dataset. 4th row: the inner and outer confidence sets produced by calibrating the smoothed*
 1329 *scores (smoothed with an isotropic Gaussian kernel of 20mm - chosen because it performed the best*
 1330 *on the learning dataset). As for the learning dataset the original scores perform very poorly and are*
 1331 *not able to separate the background from the segmented masks with confidence. Instead the distance*
 1332 *transformed scores do a very good job at segmenting the mask. Indeed they do slightly better on the*
 1333 *calibrated dataset than on the learning dataset. The smooth scores improve on the original scores*
 1334 *but do not provide as tight bounds as the distance transformed scores for neither inner nor outer*
 1335 *sets.*

1336
 1337
 1338
 1339
 1340
 1341
 1342
 1343
 1344
 1345
 1346
 1347
 1348
 1349

1350
1351

A.5.4 COMPUTING THE COVERAGE FOR THE BRAIN IMAGING DATA

1352
1353
1354
1355
1356
1357
1358

In order to study the coverage rate of the methods in the context of the brain imaging application we perform a similar validation to that described in Section 3.3 for polyps segmentation. To do so we divide the 474 subjects left, after excluding the learning dataset, into 300 calibration and 174 test images. We do this 1000 times, randomly sampling the sets of 300 and 174 images respectively and measuring the coverage in each run. We average the coverage over the 1000 runs and display the results in Figure A21. Note that unlike the box scores considered in Section 3.3, the smooth scores are not discrete so do not display discreteness issues at lower levels of coverage.

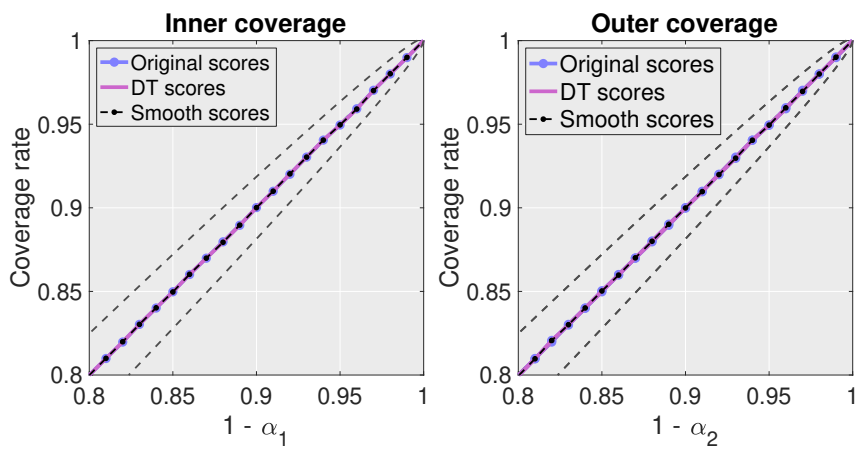
1359
1360
1361
1362
1363
1364
1365
1366
1367
1368
1369
1370
1371
1372
1373

Figure A21: Coverage levels of the inner and outer sets averaged over 1000 validations for the original, distance transformed (DT) and smoothed scores (smoothed with a full width at half maximum of 20mm). The nominal rate is achieved in all settings considered.

1374
1375
1376
1377
1378
1379
1380
1381
1382
1383
1384
1385
1386
1387
1388
1389
1390
1391
1392
1393
1394
1395
1396
1397
1398
1399
1400
1401
1402
1403

1404

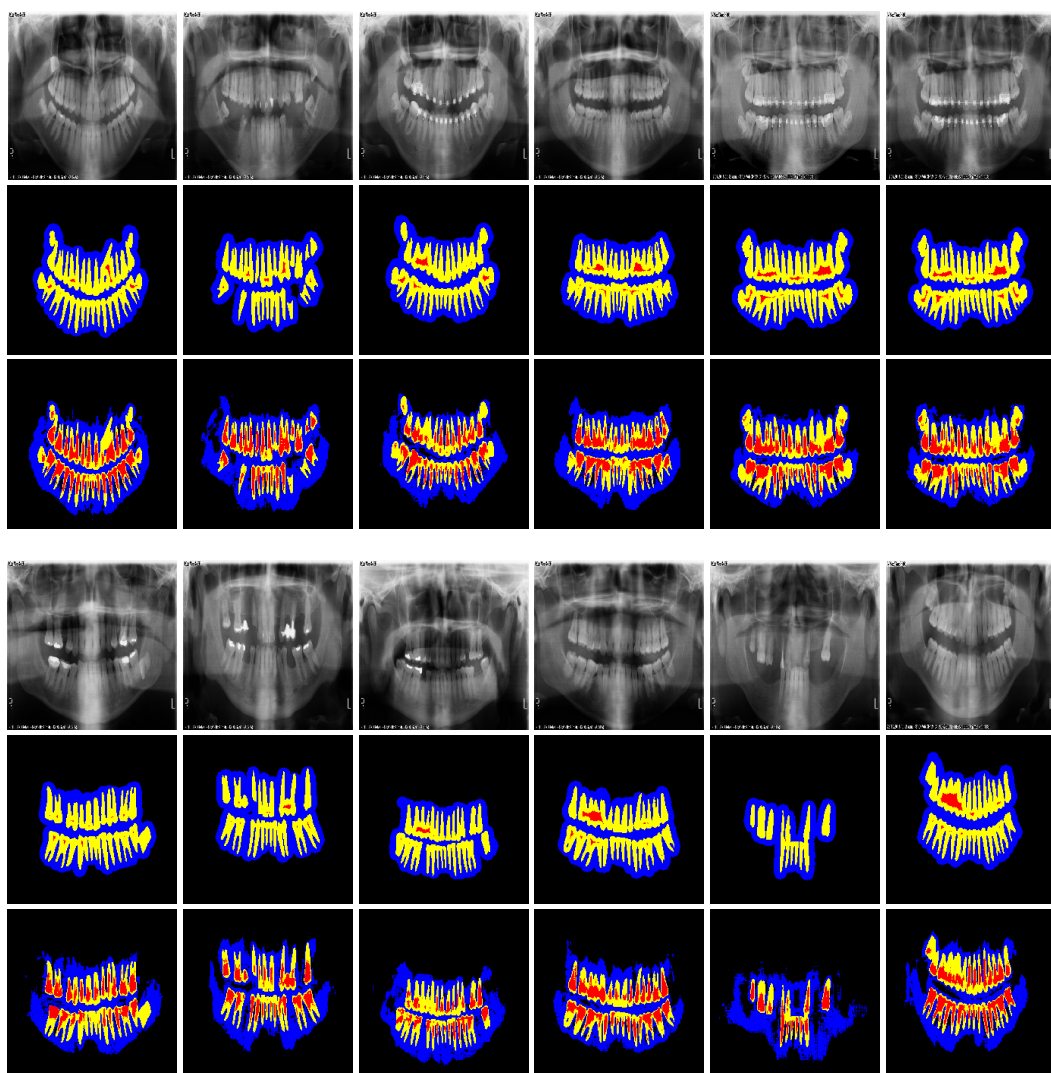
A.6 ADDITIONAL SETTINGS FOR TEETH SEGMENTATION

1405

1406

A.6.1 COMPARING ORIGINAL AND DISTANCE TRANSFORMED SCORES ON THE LEARNING
1407 DATASET

1408



1443

Figure A22: *Inner and outer confidence sets for brain mask segmentation calibrated and plotted on the learning dataset. 12 images are plotted in two sets of 6, for each set the rows are as follows. First row: original images. Second row: results of distance transformed scores - providing tight outer sets but uninformative inner sets. Third row: original scores providing looser outer sets but more informative inner sets though these can be improved by smoothing see Figure A23.*

1444

1445

1446

1447

1448

1449

1450

1451

1452

1453

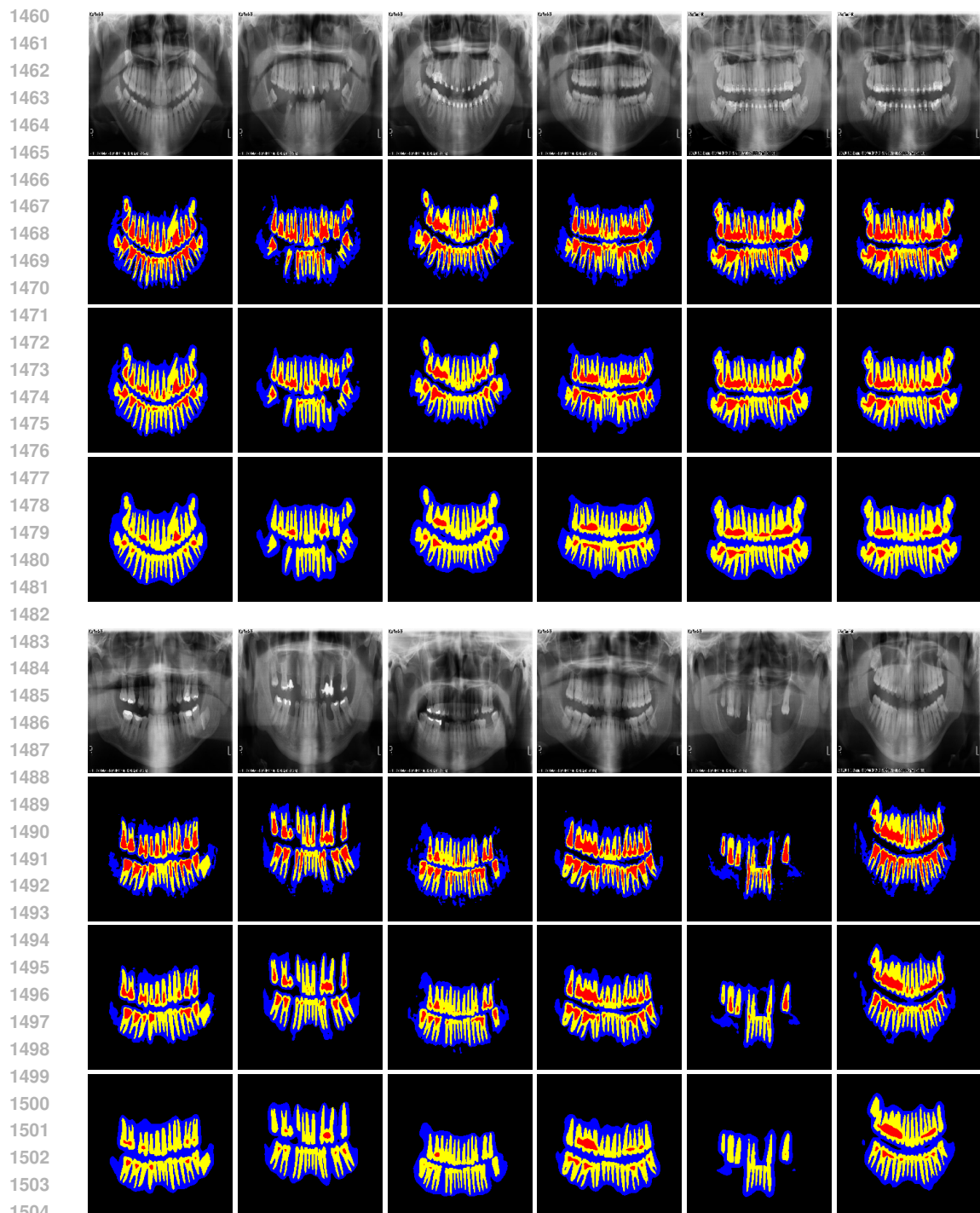
1454

1455

1456

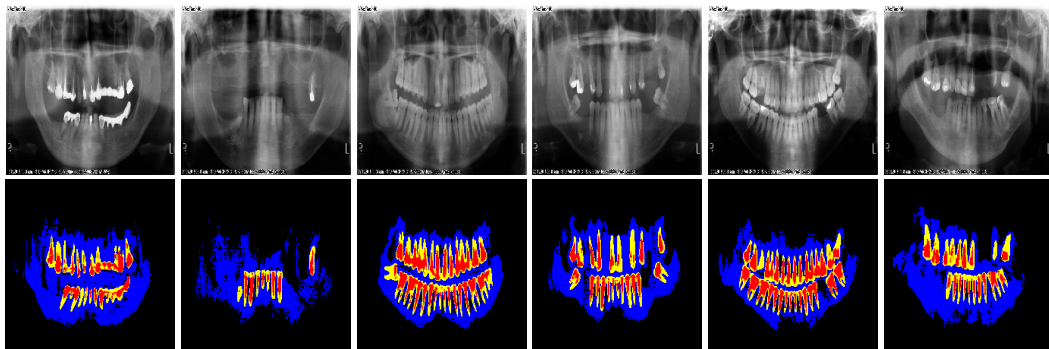
1457

1458 A.6.2 COMPARING SMOOTH TRANSFORMED SCORES ON THE LEARNING DATASET
 1459



1505 Figure A23: *Inner and outer sets computed by comparing smooth score transformations on the*
 1506 *learning dataset. Scores were smoothed using a Gaussian kernel with full width at half maximum*
 1507 *(FWHM) taking values in $\{2, 4, 8\}$. For each set of 6 the resulting inner and outer sets based*
 1508 *on increasing levels of applied smoothness are shown from top to bottom. A FWHM of 2 pixels*
 1509 *is the best for the inner set and indeed performs better than the original scores shown in Figure*
 1510 *A22. Instead an increased level of smoothness is better for the outer set, attaining comparable*
 1511 *performance to the distance transformed scores though with additional blobs.*

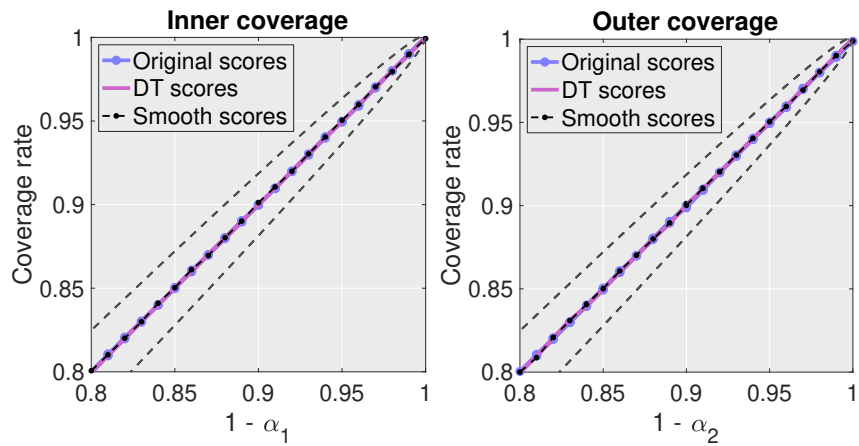
1512 A.6.3 COMPARING TO THE ORIGINAL SCORES ON THE TEST DATASET
 1513



1514
 1515
 1516
 1517
 1518
 1519
 1520
 1521
 1522
 1523
 1524
 1525
 1526
 1527 Figure A24: *Inner and outer confidence sets for brain mask segmentation computed using the original scores. The performance is less good than the score transformations optimized on the learning dataset and shown in the main text but have been included for reference. The outer sets are larger and less precise than those based on the distance transformation. The inner sets are good but not quite as good as the ones based on a small amount of smoothing.*
 1528
 1529
 1530
 1531
 1532

1533 A.6.4 COMPUTING THE COVERAGE FOR THE TEETH DATASET
 1534

1535 In order to study the coverage rate of the methods in the context of the brain imaging application we
 1536 perform a similar validation to that described in Sections 3.3 and A.5.4. To do so we divide the 198
 1537 subjects, into subsets of size 170 and 28. We do this 1000 times, randomly sampling the sets of 170
 1538 and 28 images respectively and measuring the coverage in each run. We average the coverage over
 1539 the 1000 runs and display the results in Figure A25.



1540
 1541
 1542
 1543
 1544
 1545
 1546
 1547
 1548
 1549
 1550
 1551
 1552
 1553
 1554
 1555 Figure A25: Coverage levels of the inner and outer sets averaged over 1000 validations for the original, distance transformed (DT) and smoothed scores (smoothed with a full width at half maximum of 2 pixels). The nominal rate is achieved in all settings considered.
 1556
 1557
 1558
 1559
 1560
 1561
 1562
 1563
 1564
 1565

1566 A.7 COMPARING PERFORMANCE METRICS FOR EACH SEGMENTATION MODEL
15671568 In the table we display performance metrics for each model, computed over the validation set used
1569 in each data application.1570
1571 Table 1: Performance Metrics over the validation set
1572

Model	Application	Average Dice Score	Average Precision	Average Recall
PraNet	Polyps	0.9357	0.9365	0.9200
HDBET	Brain imaging	0.97578	0.96058	0.99158
U-Net based GAN	Teeth	0.93347	0.93548	0.93236

1573
1574 A.8 ANALOGY TO FWER CONTROL
15751576 *This section formalize the analogy between coverage and FWER control.*
15771578 FAMILY-WISE ERROR RATE (FWER)
15791580 *In traditional multiple hypothesis testing Family-Wise Error Rate (FWER) is the probability of making at least one false discovery across a set of considered hypotheses. Given a multiple testing problem in which m hypotheses are tested and a multiple testing algorithm \mathcal{M} , let $V(\mathcal{M})$ denotes the resulting set of false discoveries, $R(\mathcal{M})$ the set of rejected hypotheses and T be the set of true rejections. Then the FWER is defined as:*
1581

1582
$$FWER(\mathcal{M}) := \mathbb{P}(|V(\mathcal{M})| \geq 1).$$

1583 *Then, given $\alpha > 0$, if we can guarantee that $FWER \leq \alpha$ then it follows that $R(\mathcal{M}) \subseteq T$ with probability at least $1 - \alpha$. This statement is thus analogous to the coverage guarantees which we provide in Theorems 2.1 and 2.2 in the sense that a probabilistic gaurantee on the inclusion probability is provided.*
15841585 FALSE DISCOVERY RATES AND PROPORTIONS
15861587 *Instead the false discovery proportion in the multiple testing setting for an algorithm \mathcal{M} is given by:*
1588

1589
$$FDP(\mathcal{M}) := \frac{|V(\mathcal{M})|}{|R(\mathcal{M})|} \cdot \mathbf{1}_{|R(\mathcal{M})|>0}$$

1590 *and the False Discovery Rate is given by:*
1591

1592
$$FDR(\mathcal{M}) = \mathbb{E}[FDP],$$

1593 *where $\mathbf{1}_{|R(\mathcal{M})|>0}$ is an indicator function that is 1 when $|R(\mathcal{M})| > 0$ and 0 otherwise. Controlling the FDP in probability is thus analogous to the proportion of the true mask that lies within the discovered sets, as in Bates et al. (2021) whilst controlling the FDR is instead analogous to the risk control discussed in Angelopoulos et al. (2021) in which conformal inference is used to control the expected proportion of the true mask which is discovered.*
15941595
1596
1597
1598
1599
1600
1601
1602
1603
1604
1605
1606
1607
1608
1609
1610
1611
1612
1613
1614
1615
1616
1617
1618
1619